

RL-TR-97-7
Final Technical Report
January 1997



INVESTIGATIONS OF FIBER OPTIC DELAY LINE SIGNAL PROCESSORS AND A FIBER OPTIC INTRUSION SENSOR SYSTEM

Texas A&M University

Henry F. Taylor

19970311 015

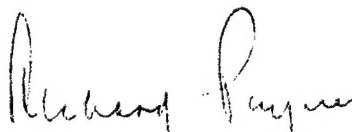
APPROVED FOR PUBLIC RELEASE; DISTRIBUTION UNLIMITED.

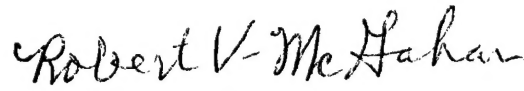
DTIC QUALITY INSPECTED 3

**Rome Laboratory
Air Force Materiel Command
Rome, New York**

This report has been reviewed by the Rome Laboratory Public Affairs Office (PA) and is releasable to the National Technical Information Service (NTIS). At NTIS it will be releasable to the general public, including foreign nations.

RL-TR-97-7 has been reviewed and is approved for publication.

APPROVED: 
DR. RICHARD PAYNE
Project Engineer

FOR THE COMMANDER: 
DR. ROBERT V. McGAHAN, Acting Director
Electromagnetics & Reliability Directorate

If your address has changed or if you wish to be removed from the Rome Laboratory mailing list, or if the addressee is no longer employed by your organization, please notify RL/80 Scott Drive, Hanscom AFB MA 01731-2909. This will assist us in maintaining a current mailing list.

Do not return copies of this report unless contractual obligations or notices on a specific document require that it be returned.

REPORT DOCUMENTATION PAGE			Form Approved OMB No. 0704-0188	
Public reporting burden for this collection of information is estimated to average 1 hour per response, including the time for reviewing instructions, searching existing data sources, gathering and maintaining the data needed, and completing and reviewing the collection of information. Send comments regarding this burden estimate or any other aspect of this collection of information, including suggestions for reducing this burden, to Washington Headquarters Services, Directorate for Information Operations and Reports, 1215 Jefferson Davis Highway, Suite 1204, Arlington, VA 22202-4302, and to the Office of Management and Budget, Paperwork Reduction Project (0704-0188), Washington, DC 20503.				
1. AGENCY USE ONLY (Leave Blank)		2. REPORT DATE January 1997		3. REPORT TYPE AND DATES COVERED Final Jan 92 - Jun 95
4. TITLE AND SUBTITLE INVESTIGATIONS OF FIBER OPTIC DELAY LINE SIGNAL PROCESSORS AND A FIBER OPTIC INTRUSION SENSOR SYSTEM			5. FUNDING NUMBERS C - F19628-92-K-0005 PE - 62702F PR - 4600 TA - 19 WU - 89	
6. AUTHOR(S) Henry F. Taylor				
7. PERFORMING ORGANIZATION NAME(S) AND ADDRESS(ES) Department of Electrical Engineering Texas A&M University College Station TX 77843			8. PERFORMING ORGANIZATION REPORT NUMBER N/A	
9. SPONSORING/MONITORING AGENCY NAME(S) AND ADDRESS(ES) Rome Laboratory/ERO 80 Scott Drive Hanscom AFB MA 01731-2909			10. SPONSORING/MONITORING AGENCY REPORT NUMBER RL-TR-97-7	
11. SUPPLEMENTARY NOTES Rome Laboratory Project Engineer: Dr. Richard Payne/ERO/(617) 377-5129				
12a. DISTRIBUTION/AVAILABILITY STATEMENT Approved for Public Release; Distribution Unlimited			12b. DISTRIBUTION CODE	
13. ABSTRACT (Maximum 200 words) A programmable fiber optic delay line using optical switches, a fiber optic delay line sequence generator, and a distributed fiber optic intrusion sensor were investigated. The programmable delay line is based upon a network of all-fiber switches connected by fibers of different lengths. The switches showed an unprecedented combination of low insertion loss, polarization independent operation, and fast switching. A 4-stage system with 16 different programmable delays was constructed. The sequence generator consists of a laser which injects optical pulses into a network of 2x2 fiber couplers connected by filters of different length. Unipolar and bipolar sequences were generated at Gbit/sec rates. The intrusion sensor system analyzed in this report is intended to detect, locate, and classify intruders over long perimeters. A range of 28 km for 100 m range resolution is predicted.				
14. SUBJECT TERMS Fiber Optics, Delay Line, Switches, Intrusion Sensor			15. NUMBER OF PAGES 72	
			16. PRICE CODE	
17. SECURITY CLASSIFICATION OF REPORT UNCLASSIFIED	18. SECURITY CLASSIFICATION OF THIS PAGE UNCLASSIFIED	19. SECURITY CLASSIFICATION OF ABSTRACT UNCLASSIFIED	20. LIMITATION OF ABSTRACT UL	

TABLE OF CONTENTS

Summary	ii
1. Introduction	1
2. Single Mode Fiber Optic Switch	5
3. Programmable Fiber-Optic Delay Line	32
4. Broadband Sequence Generator	40
5. Description of Intrusion Sensor System	45
6. Component Selection for Intrusion Sensor System	49
7. Simulations of Intrusion Sensor Performance	53
8. Comparison with Competing Intrusion Sensor Approaches ..	59
9. Conclusions	61
10. References	63

SUMMARY

A programmable fiber optic delay line using optical switches, a fiber optic delay line sequence generator, and a distributed fiber optic intrusion sensor were investigated.

The programmable delay line is based upon a network of all-fiber switches connected by fibers of different lengths. The 4-port all-fiber switches have a Mach-Zehnder interferometer configuration with a piezoelectric transducer in each arm to produce a π -radian relative phase shift. Switches constructed in the laboratory show an unprecedented combination of low (0.25 dB) insertion loss, polarization-independent operation (-21 dB worst-case crosstalk), and < 30 μ sec switching time. A 4-stage system with 16 different programmable delays was constructed.

The sequence generator consists a laser which injects optical pulses into a network of 2x2 fiber couplers connected by fibers of different lengths. Both unipolar and bipolar sequences were generated at Gbit/sec rates.

The fiber optic intrusion sensor system analyzed in this report is intended to detect, locate, and classify intruders over long perimeters. One or more fibers contained in a buried cable serve as distributed sensors. Each sensor responds to the pressure of an intruder passing over or near it, as well as to acoustic waves transmitted through the soil from more distant disturbances. After the presence of an intruder is detected, a signal processor applies signature analysis techniques to the raw sensor data to distinguish between people, animals, vehicles, and aircraft. The system is configured as a coherent optical time domain reflectometer (OTDR). Alternative system designs are described and analyzed. The baseline design makes use of a diode-pumped Nd:YAG light source, a Faraday isolator, an electrooptic modulator, a fiber coupler, a cabled single mode fiber as the sensor, and an InGaAs photodetector. A pulse of highly coherent light from the laser is coupled into the fiber, and the Rayleigh backscattered light from the fiber is converted to an electrical signal by the photodetector. A range of 28 km for 100 m range resolution and a range of 12 km for 20 m range resolution are predicted.

1. INTRODUCTION

1.1. Fiber Optic Delay Lines

It has been recognized since the mid-1970's that fiber optics technology represents an alternative to conventional means for implementing wideband signal processors [1]. Present-day fibers have time-bandwidth products of over 1,000,000, and input and output transducers (high-speed lasers and photodetectors) can operate at bandwidth in excess of 10 GHz.

It was suggested some years ago that a variable fiber optic delay line can be implemented with a multistage network of 2 X 2 optical switches connected by optical fibers [2]. The switches are operated as two-state devices, as illustrated in Fig. 1. The state of each switch is set to route the incident light to the next stage through a long or short fiber, as in Fig. 2. With N of the 2 X 2 switches, 2^N different delays can be obtained by appropriate setting of the states of the switches. Furthermore, if the length difference of the two fibers following the $j+1$ st switch is twice that of the fibers following the j th switch, the total delay is $T_0 + n\tau$, with T_0 the delay for the shortest fiber path, τ the delay difference for the two fibers connecting the first and second switches, and $n = 0, 1, 2, \dots, 2^N - 1$. Extensive investigations of the switches of Fig. 1 and the delay line system of Fig. 2 have been carried out during the course of this program.

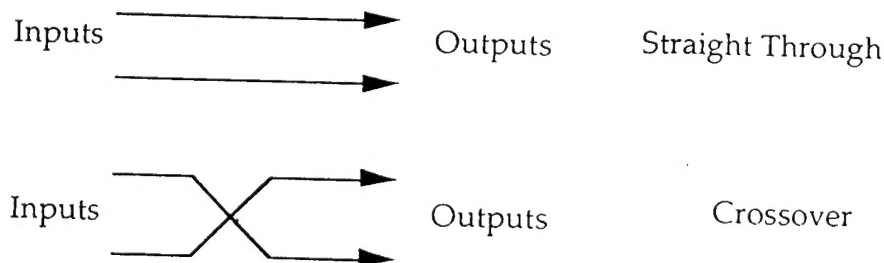


Fig. 1. States of 4-Port Optical Switches

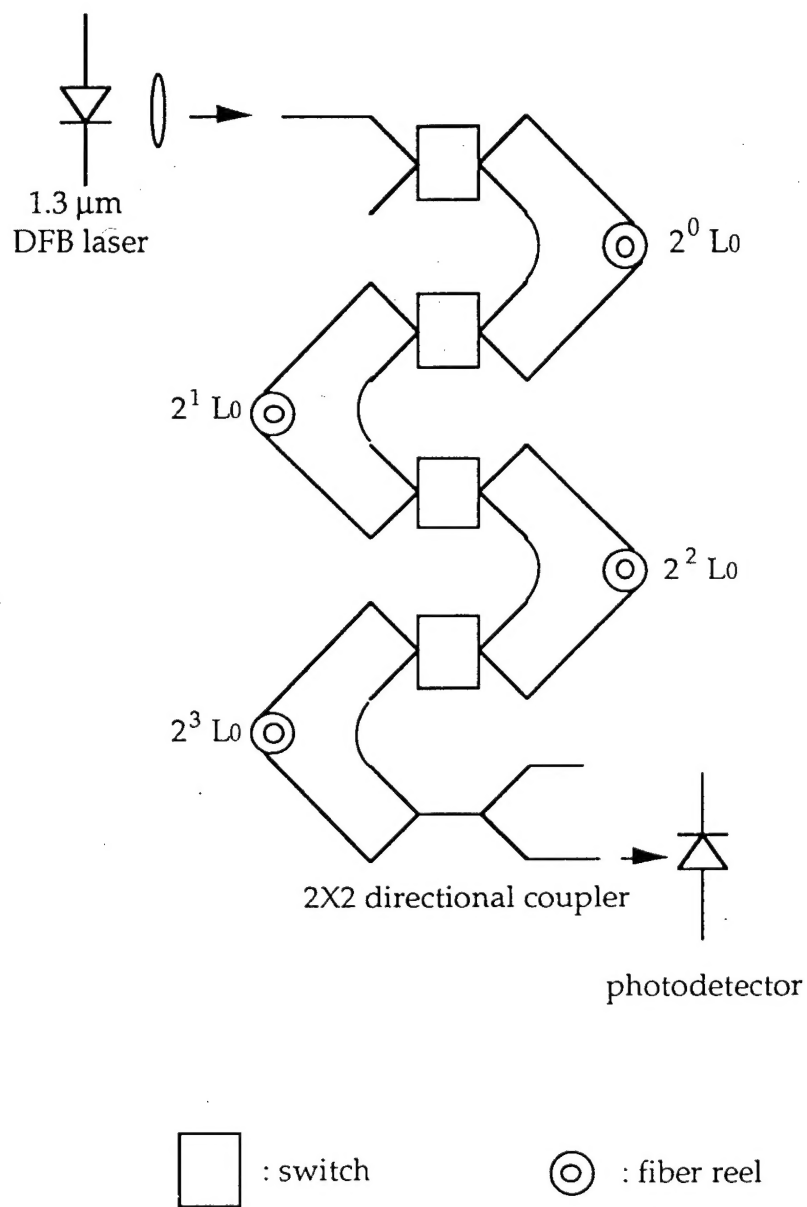


Fig. 2. Configuration for programmable delay line.

Broadband "spread spectrum" waveforms utilizing pseudorandom codes are important in Air Force radar systems, because such waveforms are difficult for the enemy to intercept and jam. Systems using pseudorandom codes must perform both signal generation and correlation (deconvolution) functions. Normally, such processors are configured as tapped delay lines, with the time-bandwidth product equal to the number of taps. Presently, charge-coupled devices, surface-acoustic-wave devices, and digital computers (microprocessors) are used in such applications, but these technologies are limited to time-bandwidth products of a few hundred at signal bandwidths of 100 Mhz. A new method for implementing broadband tapped delay line signal processors has been investigated under this program. The fiber optic processor utilizes $N \times 2$ optical couplers connected in series to generate and correlate 2^N -bit sequences.

1.1.1. Previous Implementation of All-Fiber Switch

A delay line with the configuration of Fig. 2 has been implemented with all-fiber thermooptic switches [3], as illustrated in Fig. 3. All-fiber switches were chosen over commercially available LiNbO_3 devices renders multistate networks impractical. The switch is configured as an all-fiber Mach-Zehnder interferometer arms. The characteristics of the switch are -18 dB crosstalk, 1 dB insertion loss, and 5 sec switching time. The insertion loss is far less than could be achieved with commercial single mode fiber switches, but the response of all-fiber thermooptic switches will ultimately be limited to a few milliseconds by the thermal diffusion rate in the fiber material [4]. Even this performance will be difficult to achieve in practice. Furthermore, the power dissipated by thermooptic switches is inherently high ($\sim 0.5\text{W}$), as heat must be supplied to maintain one or both states of the devices.

1.1.2 Piezoelectric Transducers

To achieve faster switching and lower power dissipation while retaining low insertion loss in the switches, piezoelectrically induced strain in all-fiber Mach-Zehnder interferometers, as shown in Fig. 4, is utilized in this project.

Piezoelectricity, which was discovered by Pierre and Jacques Curie in the 1880's, is a property of certain classes of crystalline materials. When an electric field is applied to one of these materials, the crystalline unit cell changes shape, producing dimensional changes in the material. A piezoelectric transducer is a material utilizing piezoelectricity to change its dimension by applying a voltage to it. Fig. 5 illustrates the piezoelectric action from an applied voltage.

1.2. Distributed fiber optic intrusion sensor

Illegal drugs are imported into the U. S. in vast quantities by air, sea, and land. Sensors for detecting potential smugglers are an important part of the drug interdiction effort. Most of the sensor funding in recent years has been devoted to the procurement of radars for the monitoring of private aircraft crossing into the U. S. from the Caribbean and across the Southwestern border. The deployment of balloon-mounted aerostat radars and the increased use of military aircraft for radar surveillance has greatly improved the ability of drug interdiction forces to detect and track unauthorized aircraft.

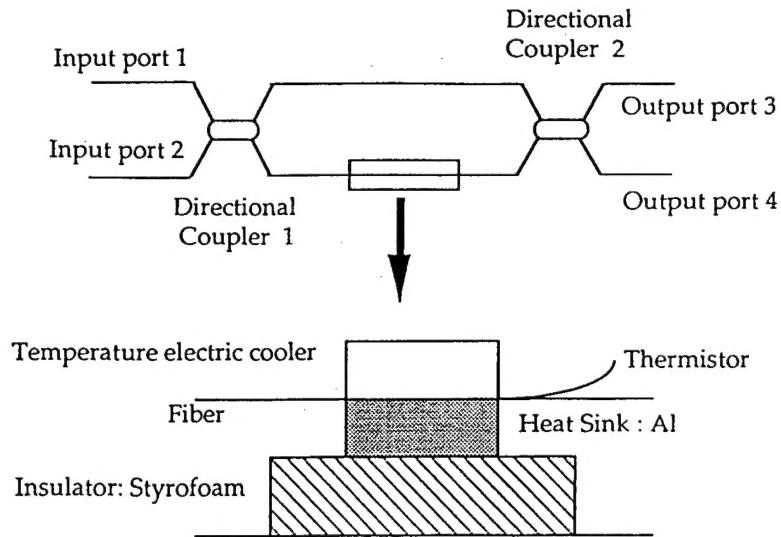


Fig. 3. All-Fiber Thermo-optic Switch

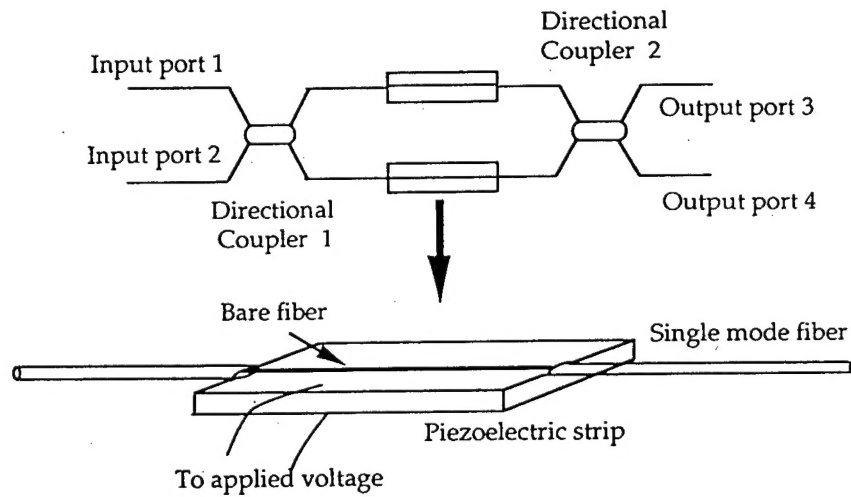


Fig. 4. Configuration for PZT-activated Fiber Switch

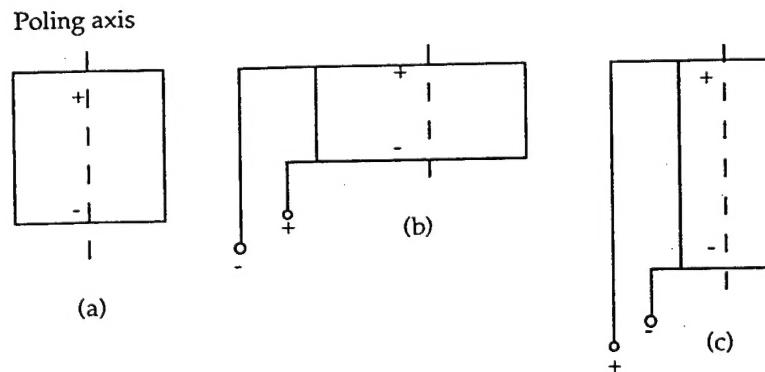


Fig. 5. Schematic Illustration of Piezoelectric Effect; (a) No Voltage on Poled Element; (b) Applied Voltage with Polarity Oposite to Poling Axis, (c) Applied Voltage of Same Polarity as Poled Element

As a result of the improved radar surveillance, smugglers are now making greater use of land and water routes. Intrusion sensors are widely used for the monitoring of land routes in support of law enforcement efforts. However, present seismic, magnetic, and infrared sensors are expensive, provide limited area coverage, are difficult to conceal, and are subject to high false-alarm rates. It is widely appreciated that most smugglers crossing into the U. S. from Mexico or Canada in land vehicles, on foot, or in boats go undetected. This situation might be dramatically improved through the availability of more effective, less expensive sensors.

With such an objective in mind, the use of fiber optic sensors for drug interdiction has been investigated at Texas A&M University over the past three years. During the course of this investigation, a novel approach based on coherent optical time domain reflectometry (coherent OTDR) was conceived and preliminary experiments to test some key technical issues associated with the approach were carried out. It was found using a Michelson interferometer configuration that an intruder on foot induces large (several π -radian) phase shifts in an optical carrier propagating in a cabled fiber buried 30 cm (1') deep in clay soil. The sensitivity is so great that an intruder who walks within 2 m of the buried cable is easily detected. In another experiment, it was confirmed that a localized phase perturbation in a long fiber can be located as well as detected with a coherent OTDR. Here, a spectrally pure laser and a Bragg cell were used to produce a coherent light pulse which was coupled into the fiber. The coherent OTDR output consisted of a moving-time-window interference pattern of Rayleigh-backscattered light from different parts of the fiber. A phase perturbation caused a change in the signature at a particular time delay corresponding to the location of the perturbation. The experiment demonstrated that the coherent OTDR can detect perturbations in a fiber that are much too small to be observed with a conventional OTDR.

The experimental results have been encouraging, and in Sept. 1993 ARPA initiated a program with the U. S. Army Communications -Electronics Command and Texas A&M University to investigate the potential for practical exploitation of the technology. The results of that study are described in this report.

2. SINGLE MODE FIBER OPTIC SWITCH

Four-port optical switches could find widespread application in fiber communications systems to provide fault tolerance as well as for signal routing. Integrated optical switches activated thermooptically [4] and electrooptically [5] are currently available commercially. However, when switching speed, insertion loss, crosstalk, and cost are considered, present optical switches do not measure up to their electronic counterparts. As a consequence, optical switches are still not widely used in fiber communications, where switching in the electronic domain is generally preferred even though this requires additional optical to electrical to optical conversion steps.

The all-fiber Mach-Zehnder interferometer is an alternative to integrated optics for implementation of four-port optical switches with single mode fiber input and output ports. Tuning between binary states of the switch is accomplished by changing the relative phase difference between the interferometer arms by π radians. A thermally actuated switch of this type which utilized resistive heating of one of the fiber arms has been reported [3]. However, thermal diffusion from the surface to the core of a 125 μm silica fiber limits the switching time constant to a few msec [4], and even this performance is difficult to achieve in practice. Furthermore, the

heater must be operated continuously to maintain the switch at a particular operating point, resulting in substantial electrical power consumption even in a standby mode of operation.

This chapter describes the design and performance of a new all-fiber switch, illustrated schematically in Fig. 4. The switch is produced by splicing together two commercial 2 X 2 fiber directional couplers to form a Mac-Zehnder interferometer. High speed is achieved using small piezoelectric elements to change the relative path lengths in the interferometer arms. Low optical insertion loss results from the excellent loss characteristics of the fiber couplers and the splices. Low crosstalk is a consequence of the tight splitting-ratio tolerance in the couplers and very close matching of the optical paths in the interferometer. Polarization independence is attained by avoiding twists and asymmetric stresses in the interferometer arms.

2.1 Crosstalk

Crosstalk is defined as the maximum ratio of the output power from port i to that from output port j , when light is coupled into one input port with arbitrary polarization and the switch is tuned to maximize the power from port j . That is $\text{crosstalk} = 10 \log \left(\frac{P_i}{P_j} \right)$, when P_j is tuned to maximum.

Fig. 6 shows the setup for characterizing the crosstalk of a 2X2 optical switch. To excite a TE mode with the input light, a polarizing beam splitter (PBS) is inserted between the light source and the objective lens. If a TM mode is to be excited, a half-wave plate is added between the PBS and objective lens.

Three important factors determine the crosstalk of the all-fiber Mach-Zehnder switch-the splitting ratio of the fiber couplers, the optical path length match of the interferometer, and the polarization states of the light in the interferometer arms.

2.1.1 Splitting ratio of the fiber couplers

Crosstalk performance of the switch is limited by deviations in the splitting ratio of the fiber couplers from the desired condition of equal power division. Referring to Fig. 7, if we omit the time-dependence of the electric fields, $e^{j\omega t}$, then the outputs of coupler 1 are

$$E_1' = a E_0 \quad (1a)$$

$$E_2 = -j b E_0 \quad (1b)$$

where a and b are electric fields splitting ratio. Optical power conservation requires that $a^2 + b^2 = 1$. The $\pi/2$ phase difference comes from energy conservation of coupling mode theory [6]. The electric fields before the coupler 2 are

$$E_1' = a E_0 e^{jBL} \quad (2a)$$

$$E_2' = -jb E_0 e^{jB(L+\Delta L)} \quad (2b)$$

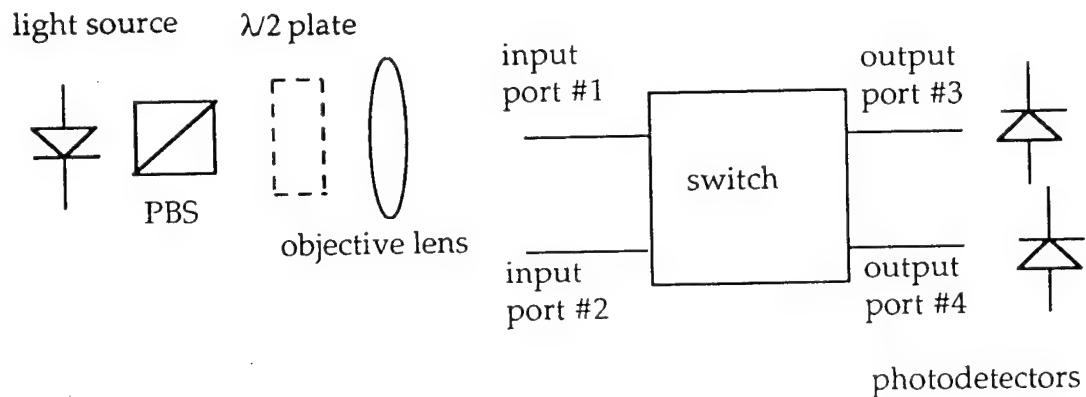


Fig. 6. Arrangement for Characterizing Crosstalk of 2x2 Optical Switch

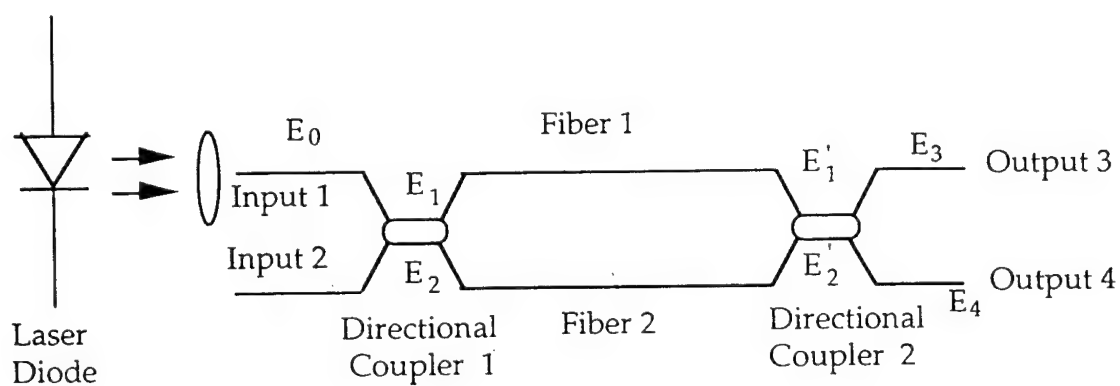


Fig. 7. 2x2 Switch Configured as Mach-Zehnder Interferometer in Single Mode Fiber

where β is the propagation constant. Then the electric fields passing through coupler 2 are

$$E_3 = a E'_1 - j b E'_2 \quad (3a)$$

$$E_4 = -j b E'_1 + a E'_2 \quad (3b)$$

The optical powers at the output of the interferometer can be calculated by determining the absolute square of E_3 and E_4

$$P_3 = [a^4 + b^4 - 2a^2b^2 \cos(\beta\Delta L)]E_0^2 \quad (4a)$$

$$P_4 = [2a^2b^2 + 2a^2b^2 \cos(\beta\Delta L)]E_0^2 \quad (4b)$$

If the splitting ratio $a^2 = 0.5 + \delta$ and $b^2 = 0.5 - \delta$ in each fiber coupler, then the maximum optical power from port #4 is $1 - 4\delta^2$ for small δ . Specifications for the couplers we used in this project (AOFR model S50-13-10-a) indicate that $\delta \leq 0.02$, so that the maximum crosstalk due to splitting ratio mismatch would be 0.0016, or -28 dB.

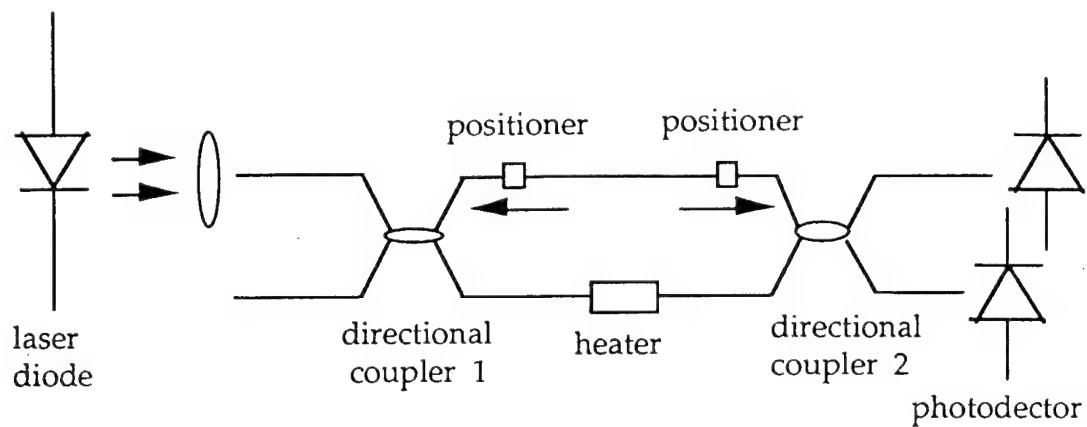
2.1.2 Optical path length match.

For use of the switch with semiconductor laser light sources, best crosstalk performance requires that the optical path lengths of the interferometer arms be very closely matched. Otherwise, voltages corresponding to the two states of the switch will differ for the different longitudinal modes of the laser. This is particularly important for Fabry-Perot lasers, but must also be considered for distributed feedback lasers when switch crosstalk levels below -20dB are sought.

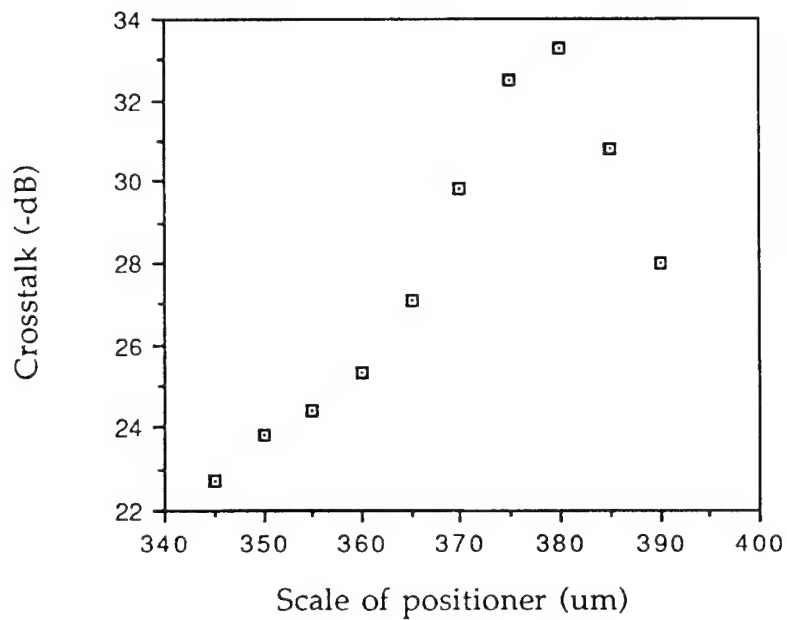
Fig. 8 shows a setup for determining the crosstalk of an all-fiber Mach-Zehnder interferometer as a function of optical path length difference. The Mach-Zehnder interferometer was prepared with length differences of the two arms of less than 2 mm, the shorter arm was attached to two linear positioners, and the longer arm to a heater. The optical path length difference was changed by adjusting the linear positioners along the fiber axis and the phase was changed through 2π radians via thermo-optic effect to determine the crosstalk. With a DFB laser diode as the light source, the lowest crosstalk is -33 dB at 382 μm of the positioner scale, which corresponds to the case that the optical path length is matched. It was also found that -24 dB crosstalk can be achieved by matching the interferometer arm lengths to within 30 μm .

2.1.3 OCDR for optical path difference measurement

In this work, an optical coherence domain reflectometer arrangement [7], as shown in Fig. 9, was used to measure the length difference for the two arms of each coupler which would ultimately be joined to form a switch. Light from a pigtailed light emitting diode (LED0) is divided into two equal parts by a 50:50 fiber directional coupler C_1 . One of the directional coupler outputs passes out of the fiber, is collected by an objective lens, and is reflected back into the same fiber by a movable mirror. The other output from C_1 serves as the input to the directional coupler which will be prepared for the Mach-Zehnder interferometer. This light is partially



(a)



(b)

Fig. 8. (a) Setup for determining crosstalk of an all-fiber Mach-Zehnder interferometer as a function of optical path length difference. (b) Dependence of crosstalk on location of positioner which stretches one arm of interferometer.

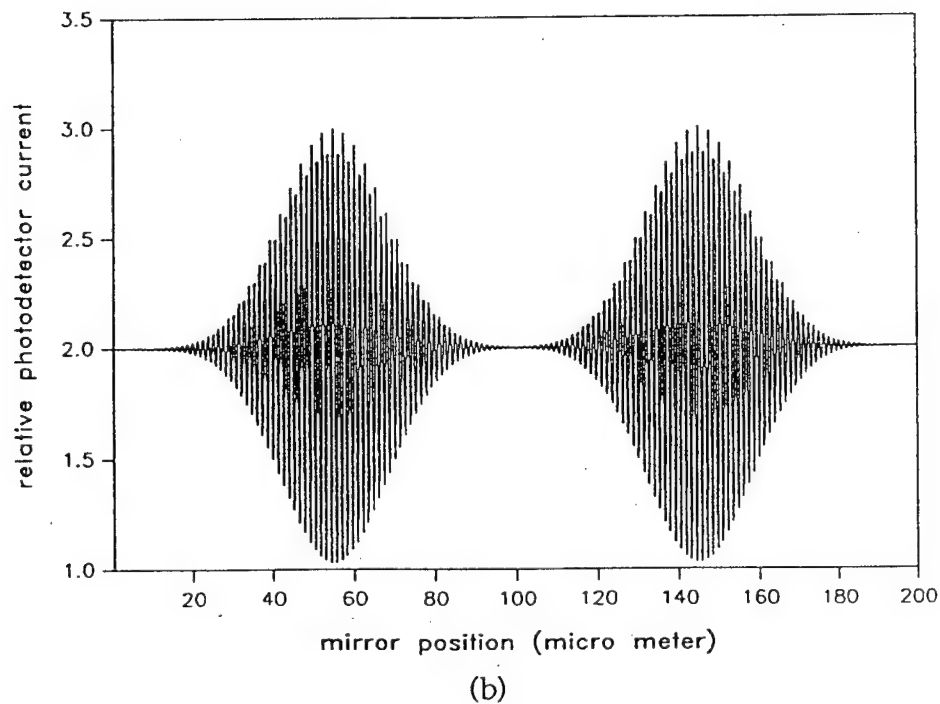
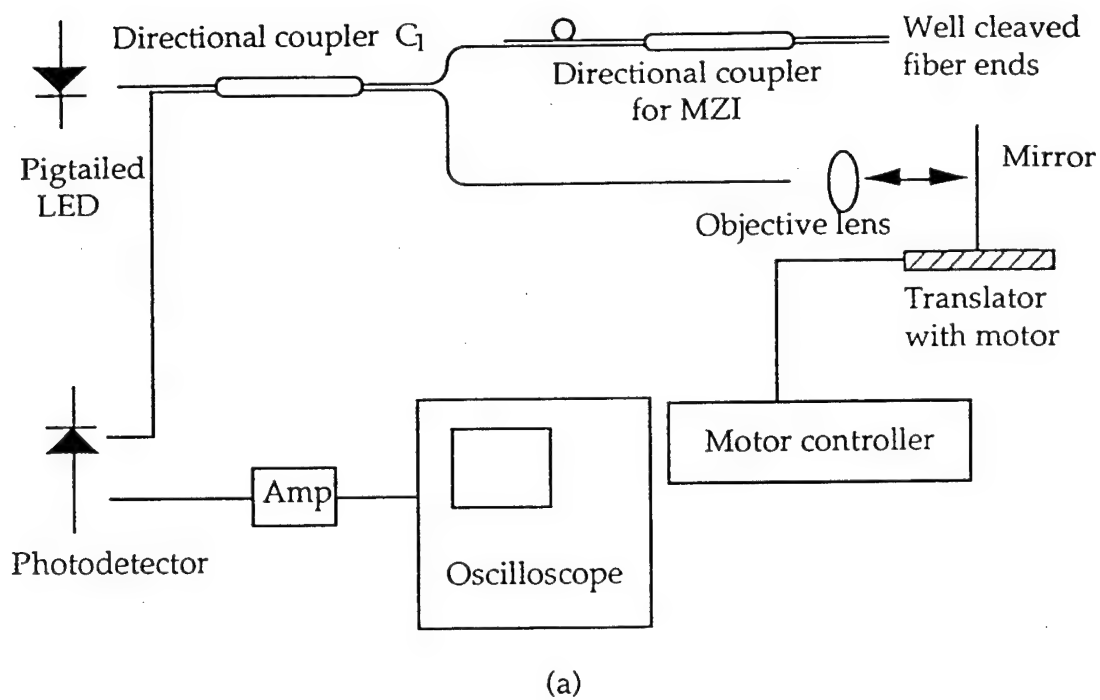


Fig. 9. (a) Optical coherence domain reflectometer for preparing length match directional couplers. (b) Dependence of photodetector signal on mirror position.

reflected at two well-cleaved fiber ends. This reflected light is detected by a photodetector and the signal is amplified before being displayed on an oscilloscope. The output current of the photodetector I_d is function of the mirror position l [8], [9] given by

$$I_d(I) = k\{2 + \gamma(l - l_1)\cos[2\pi(l - l_1)/\lambda] + \gamma(l - l_2)/\lambda\} \quad (5)$$

where k is a constant, λ is the average wavelength of the LED, l_1 and l_2 are the lengths of the fiber arms to be determined, and γ is the degree of coherence of the light. Assuming that the spectrum of the LED is Gaussian in shape, then

$$\gamma(l) = \exp\left[-\left(\frac{\pi l}{2\sqrt{\ln 2}L_c}\right)^2\right] \quad (6)$$

where L_c is the coherence length of the LED.

From Eqs. (5) and (6), it is evident that an interference pattern with high visibility will be observed when either $|l - l_1|$ or $|l - l_2|$ is smaller than L_c . Thus moving the mirror as illustrated in Fig. 9 (a) will produce a fringe pattern on the oscilloscope when the variable optical path l is closely matched to either one of the fiber arms. The length difference of the two fiber arms is the distance by which the mirror is translated between the two interference peaks divided by the effective refractive index of the fiber. Spatial resolution is about 5 μm using light source which has a 25 μm coherence length. After the length difference of the two fiber couplers is measured, the fiber in one of the couplers is cleaved until the two couplers have a closely matched length difference for the two arms. Then the two couplers are jointed in series by fusion splicing, the longer arm of one being connected to the shorter arm of the other, and vice versa.

2.1.4 Polarization states of the two interference lights

Polarization is another factor which affects crosstalk. If the optical inputs to the second coupler were orthogonally polarized, then no switching at all would be observed. Moreover, the birefringence effect in the interferometer arms can result in a nominal phase difference which is dependent on incident polarization. As a practical matter, twisting and straining of the interferometer arms were avoided in assembly of the switch to minimize polarization conversion [10], [11].

2.1.5 Performance

Two switches were made for a crosstalk performance test, using a 1.3 μm distributed feedback laser as the light source. Crosstalk performance of switch #1 is summarized in Table 1. With the setup of Fig. 6, linearly polarized light was coupled into one of the inputs, and the power from each port was measured for both states of the switch. This was repeated for each of four input conditions corresponding to two orthogonal polarizations and two input ports. data was taken using both piezoelectric and thermal tuning for comparison. Worst case crosstalk was -22 dB in both cases.

Table 2 shows crosstalk performance of switch #2 with piezoelectric tuning at three different temperatures. Worst case crosstalk was -21 dB. It should be noted that the applied

Table 1. Crosstalk performance of switch #1 (dB). (a) Piezoelectric activation. $V_a = -30.5$ V for $1 \rightarrow 3$ and $2 \rightarrow 4$ (straight through), $V_b = 26.6$ V for $1 \rightarrow 4$ and $2 \rightarrow 3$ (crossover). (b) thermooptic activation.

	input port #1		input port #2	
	TE	TM	TE	TM
output port #3	-24.6	-25.1	-21.5	-21.0
output port #4	-21.7	-22.0	-24.9	-22.0

(a)

	input port #1		input port #2	
	TE	TM	TE	TM
output port #3	-25.5	-22.4	-23.2	-23.5
output port #4	-23.2	-22.5	-22.9	-25.5

(b)

Table 2. Crosstalk performance of switch #2 (dB).

T=22.5°C	input port #1		input port #2	
	TE	TM	TE	TM
output port #3	-28.1	-27.1	-24.4	-27.4
output port #4	-26.1	-26.2	-25.1	-26.9

T=52.6°C	input port #1		input port #2	
	TE	TM	TE	TM
output port #3	-23.2	-21.1	-21.3	-22.4
output port #4	-23.6	-21.7	-21.7	-23.2

T=70.4°C	input port #1		input port #2	
	TE	TM	TE	TM
output port #3	-21.0	-22.5	-21.2	-21.3
output port #4	-21.3	-21.4	-21.3	-22.2

voltages needed to operate switch #2 as a binary state switch changed drastically with temperature. It was found that the nominal phase difference in the interferometer arms was not thermally stable, as will be discussed in section 2.5.

2.2 Switching Time

2.2.1 Phase modulator design

Piezoelectrically activated phase modulators have been studied for application in fiber-optic gyroscopes and communication systems [12 - 14]. However, most relevant articles deal with frequency domain response, rather than time domain as is the concern in this project. To suppress resonances and hold the stress simultaneously is the challenge for designing an optimal time domain phase modulator.

Fig. 10 shows the fiber inside a cylindrical piezoelectric transducer, a design which might be expected to provide symmetric stress and minimal polarization disturbance. However, experiments show that the switching is strongly affected by acoustic resonances inside the cylinder. Fig. 11 shows a configuration in which two small rings are used to hold the fiber, trying to avoid acoustic resonances and retain symmetric stress. When this design was tried experimentally, however, it was found that strong transverse vibrations disturb the outputs. Fig. 12 shows a design in which the fiber is glued on a plate type PZT-4 with epoxy. However, in this case it is found that strong acoustic waves still exist on the PZT, and the response time is slow because the epoxy is too rigid to be expand in a short time. Finally we find an ideal design, as shown in Fig. 13, which is gluing the fiber with a thin layer of cyanacrylate adhesive on a 2.5 cm X 1.0 cm X 0.5 mm plate type PZT-4. Small acoustic resonance waves can be eliminated by putting the piezoelectric transducers in damping oil, as shown in Fig. 14.

2.2.2 Switching time limit

Changing the time scale of Fig. 14, the observed 10% - 90% switching time for both the voltage and the optical output of the switch was 30 μ sec, as shown in Fig. 15. This is the time required to charge the 11 nF capacitance of the piezoelectric strips with the switching circuit. A second factor related to the response speed of the device is the acoustic wave behavior in the piezoelectric transducers and the fibers.

To investigate the acoustic response of the transducer, a model of forced longitudinal vibration of a free-standing bar with structural damping [15], [16], as shown in Fig. 16, is developed. Damping can be included in the complex Young's modulus E' where

$$E' = E (1 + j \eta) \quad (7)$$

The parameter η is the structure loss factor. The longitudinal wave equation is

$$E(1 + j\eta) \frac{\partial^2 \xi}{\partial x^2} = ps \frac{\partial^2 \xi}{\partial t^2} \quad (8)$$

where ξ is the displacement, p is the density, and s is the cross section area of the bar. The solution can be written

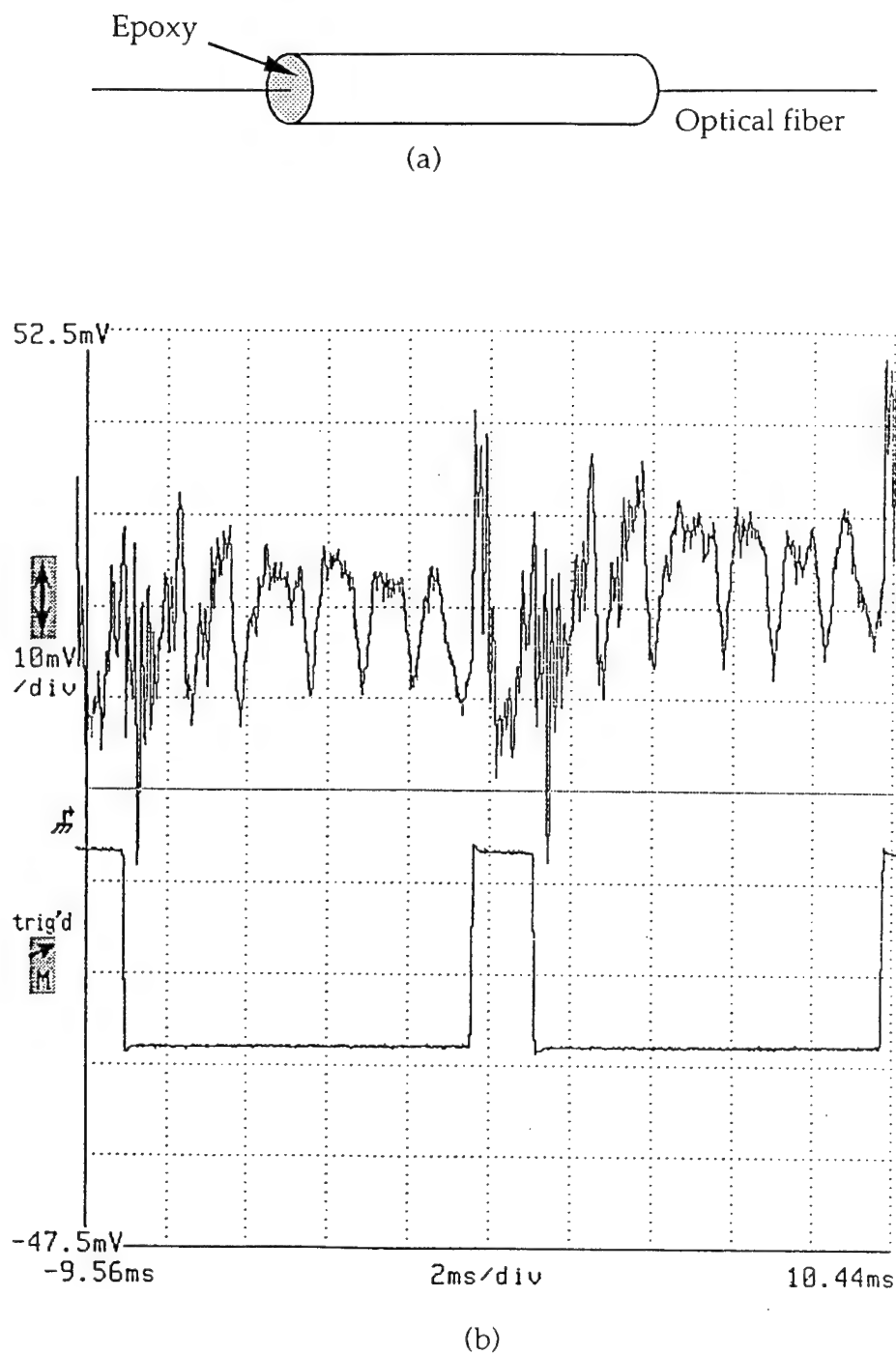


Fig. 10. (a) Phase modulator design: bare fiber inside a cylinder type PZT (length: 4.4 cm, outer diameter: 6.4 mm, and wall thickness: 1.0 mm). (b) The upper trace is the optical output and the lower trace is the applied voltage.

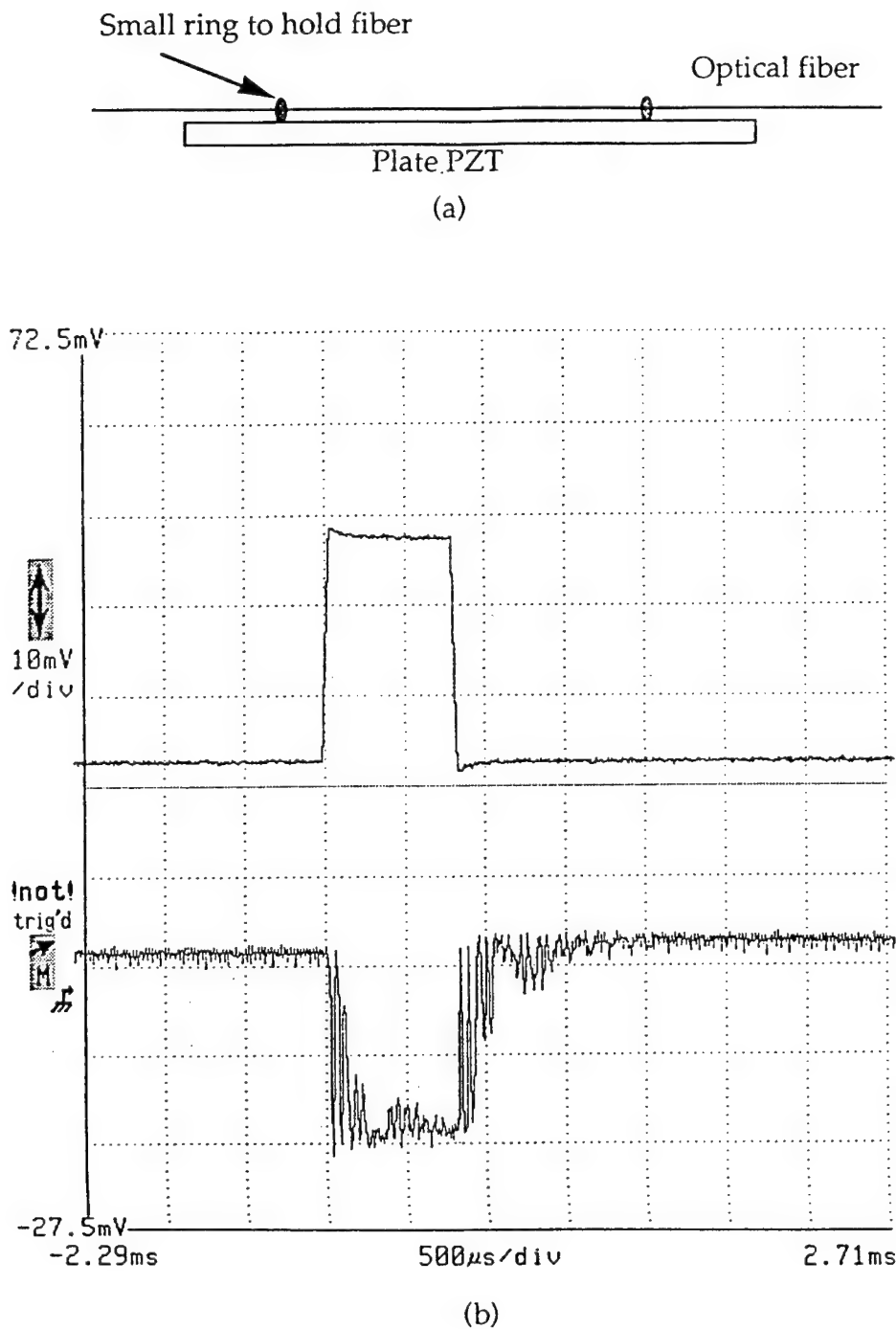


Fig. 11. (a) Phase modulator design: two small rings holding the fiber on a 7.9 cm X 6.4 mm X 1.0 mm plate type PZT. (b) The optical output is the lower trace.

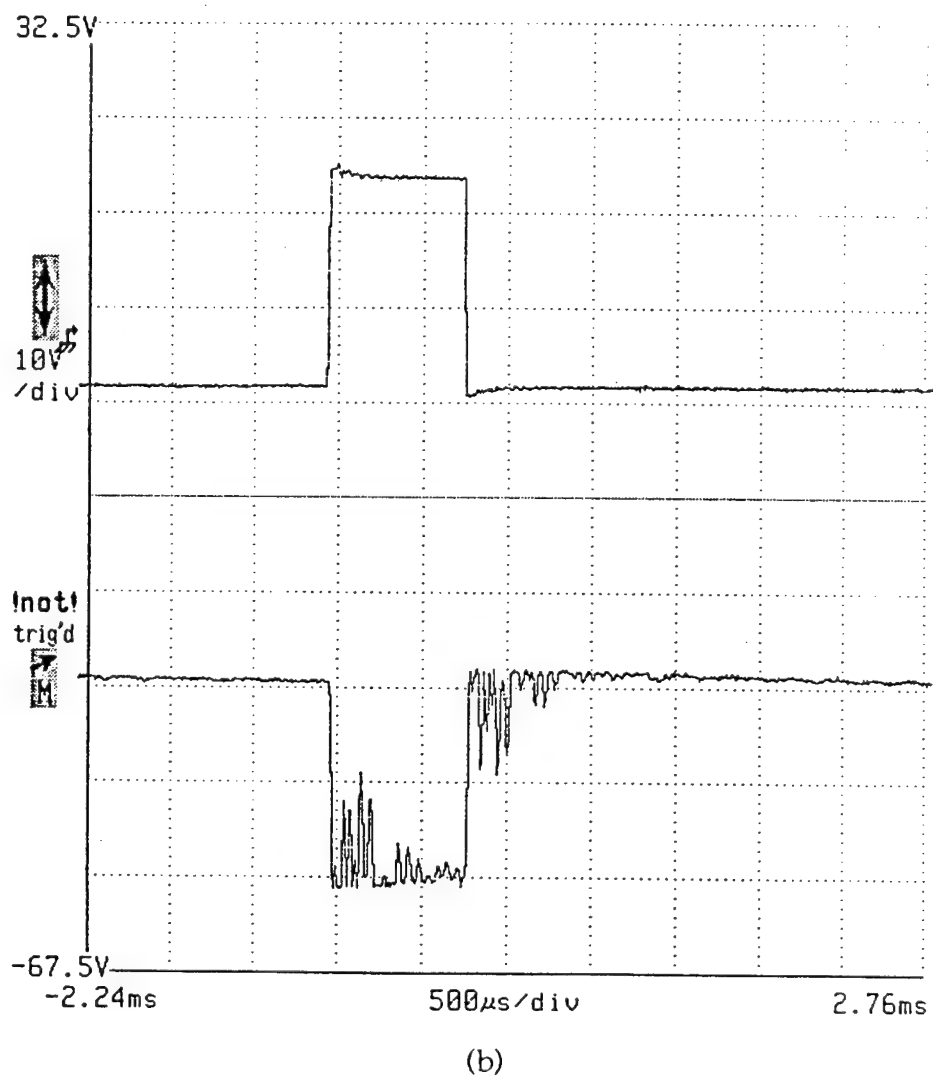
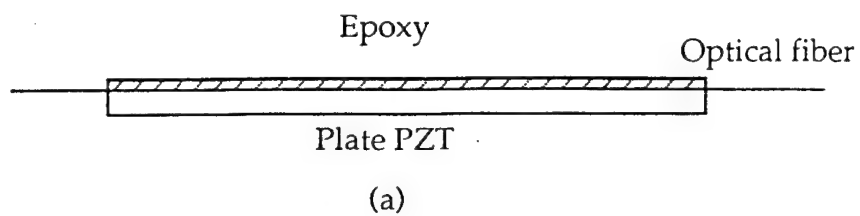


Fig. 12. (a) Phase modulator design: gluing the bare fiber with epoxy on a 2.5 cm X 1.0 cm X 1.0 mm plate type PZT. (b) The optical output is the lower trace.

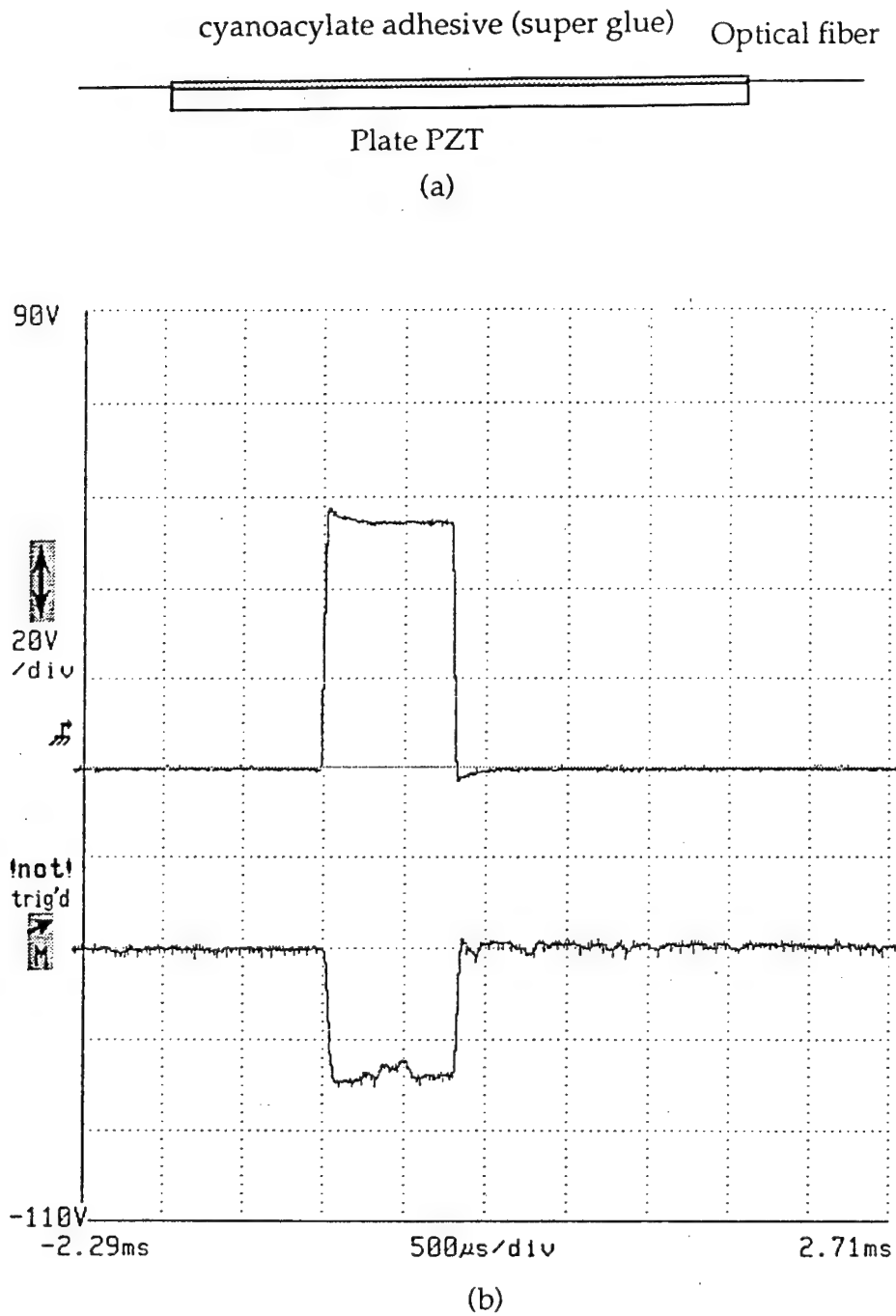


Fig. 13. (a) Phase modulator design: gluing the bare fiber with cyanoacrylate adhesive on a 2.5 cm X 1.0 cm X 0.5 mm plate type PZT-4. (b) The optical output is the lower trace.

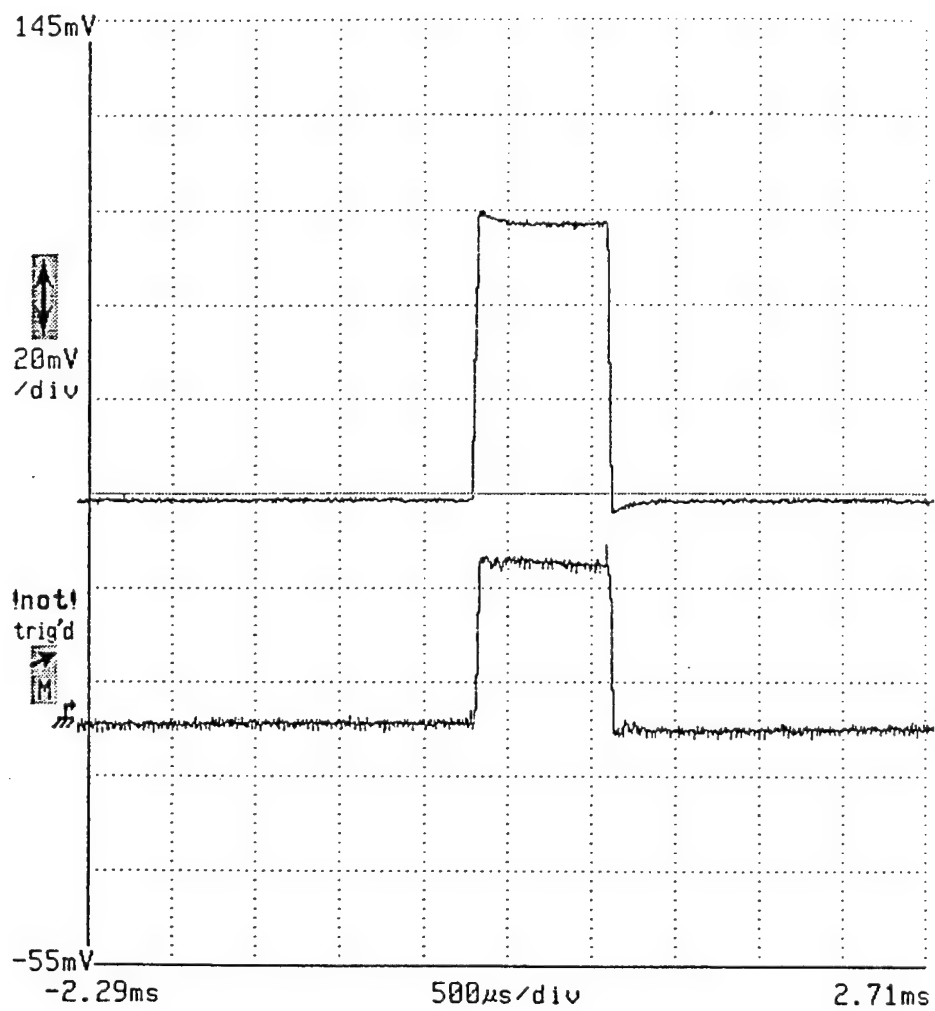


Fig. 14. The switching of the phase modulator of Fig. 13 with damping oil. The resonance waves are suppressed in the optical output (lower trace).

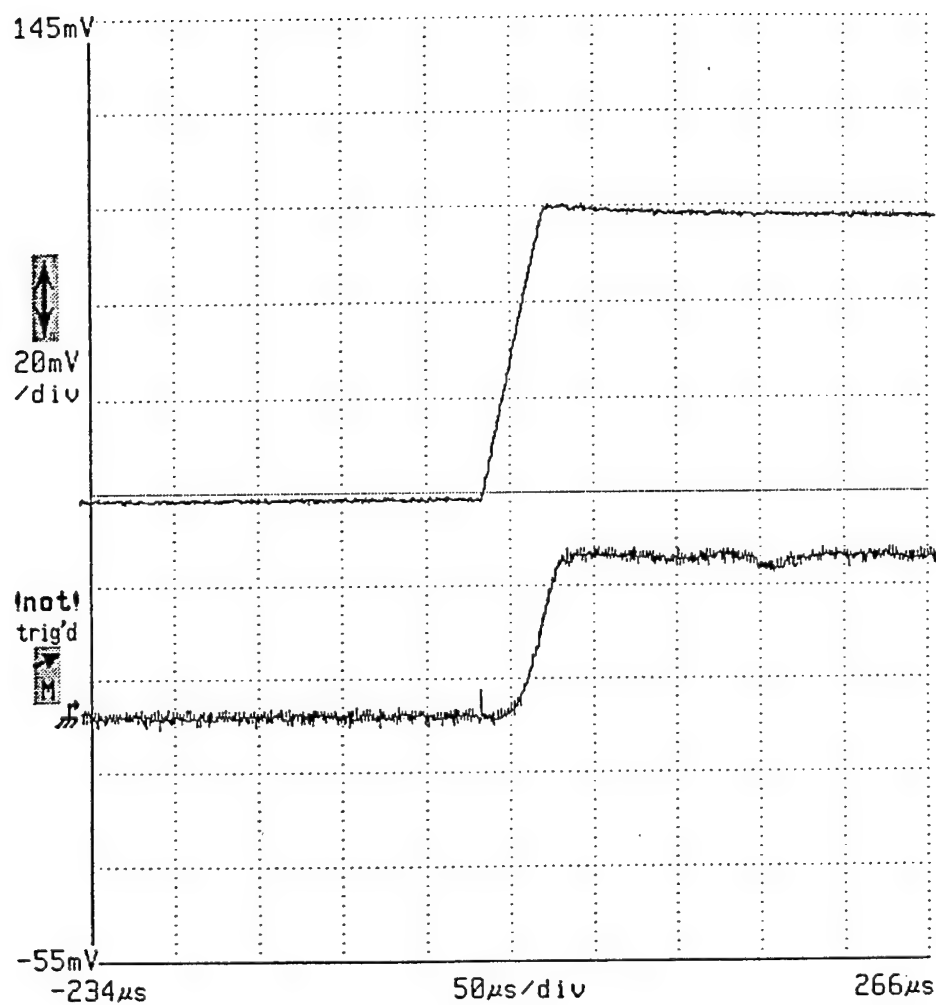


Fig. 15. Oscilloscope traces illustrating a 30 μ sec switching time. The upper trace is the voltage across the piezoelectric strips and the lower trace is the optical output from the port of the switch initially in the "off" position.

$$\xi(x, t) \cong A e^{j(\omega t - kx)} + B e^{j(\omega t + kx)} \quad (9)$$

$k = (ps\omega^2 / E(1 + j\eta))^{1/2} = (\omega / c)(1 + j\eta)^{-1/2}$ and c is the acoustic wave velocity. The bar is forced at $x=L/2$ with $Fe^{j\omega t}$ and at $x=L/2$ with $-Fe^{j\omega t}$. The expressions for the boundary conditions are

$$Fe^{j\omega t} = E's \frac{\partial \xi(-L/2, t)}{\partial x} \quad (10 a)$$

$$-Fe^{j\omega t} = E's \frac{\partial \xi(L/2, t)}{\partial x} \quad (10 b)$$

The total length change $\Delta\xi$ will be

$$\begin{aligned} \Delta\xi(t) &= -\xi(L/2, t) + \xi(-L/2, t) \\ &= \frac{2F}{jE'sk} \frac{(e^{jkL} + e^{-jkL} - 2)}{(e^{jkL} - e^{-jkL})} e^{j\omega n'} \end{aligned} \quad (12)$$

Assuming the response of the PZT to the applied voltage is linear, then the driving waveform is the same as that of the applied voltage, which is illustrated in Fig. 17. The driving in force waveform can be written in Fourier series where $\omega_0 = 2\pi/T$, and 2τ is the time required for charging the piezoelectric transducer. The displacement due to the applied voltage is

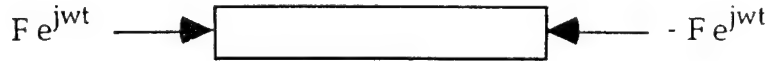


Fig. 16. Model of Forced Longitudinal Vibration of a Free-Standing Bar

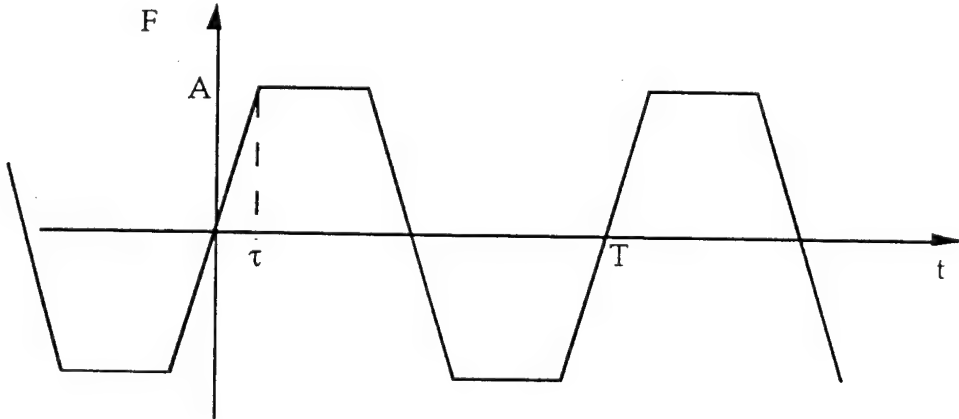


Fig. 17. Waveform of the Driving Force

$$\Delta\xi(t) = \sum_{n=-\infty}^{\infty} \frac{-8A \sin(\omega_n t) (e^{jk n^L} + e^{-jk n^L} - 2)}{T\tau\omega_n 2E'sk_n (e^{jk n^L} - e^{-jk n^L})} ej\omega_n t, \quad n \text{ is odd} \quad (14)$$

For a 2.0 cm X 5.0 mm X 0.25 mm PZT-5H piezoelectric transducer, E is 6.1×10^{10} N/m², c is 2.82×10^3 m/sec, and s is 1.27×10^{-6} m². The displacement of each piezoelectric transducer needed to induce $\pi/2$ phase shift in the optical fiber is

$$\begin{aligned} \Delta\xi\pi/2 &= \left(\frac{\lambda}{2}\right)X\left(\frac{1}{n}\right)X\left(\frac{1}{0.78}\right)X\left(\frac{1}{2}\right) \\ &= 0.29 \mu\text{m}, \text{ for } \lambda = 1.3 \mu\text{m} \end{aligned} \quad (15)$$

where n is 1.45, the effective refractive index of the optical fiber, and 0.78 is the effective optical path length change due to fiber axis expansion/contraction, which will be discussed in the next section. The amplitude of the driving force is $A=Es \Delta\xi_{\pi/2}/L=1.1$ N.

The results of computer simulations of piezoelectric transducer motion are shown in Fig. 18, 19, and 20. The longitudinal vibration is not serious with waveform without much disturbance. The applied voltage has stronger high frequency components with shorter charging time. However, the piezoelectric transducer has only weak response to frequencies higher than twice its resonance frequency because high frequencies are seriously suppressed by the piezoelectric transducer damping mechanism. The remaining high frequencies of the applied voltage waveform around the PZT resonance frequency would trigger PZT resonant motions. Thus, with 3 μ sec charging time the piezoelectric transducer is not able to follow the applied voltage waveform in such a short time, and serious resonant waves disturb the switching. The resonant waves can be suppressed by increasing η at the expense of longer switching time and larger applied voltage amplitude.

From these simulations and analysis, it is concluded that faster switching speed can be achieved with short charging time and strong damping. Fig. 21 shows switching with 3 μ sec charging time with insufficient damping, and Fig. 22 is damped by silicone glue containing the piezoelectric transducers as well as the fibers. An 8 μ sec switching time is displayed in Fig. 23, which is the shortest switching time achieved with the PZT plate phase modulator, and is in agreement with theoretical analysis.

It should be noted that even though an 8 μ sec switching time is achieved by the arrangement of Fig. 24, the polarization is very easily disturbed due to asymmetrical stress along the fiber axis and the switching voltage is four times larger than with oil damping.

2.3 Switching Voltage

The optical phase change due to stretch a section of fiber is

$$\Delta\Phi = \frac{2\pi}{\lambda} (n\Delta l + \Delta n l) \quad (16)$$

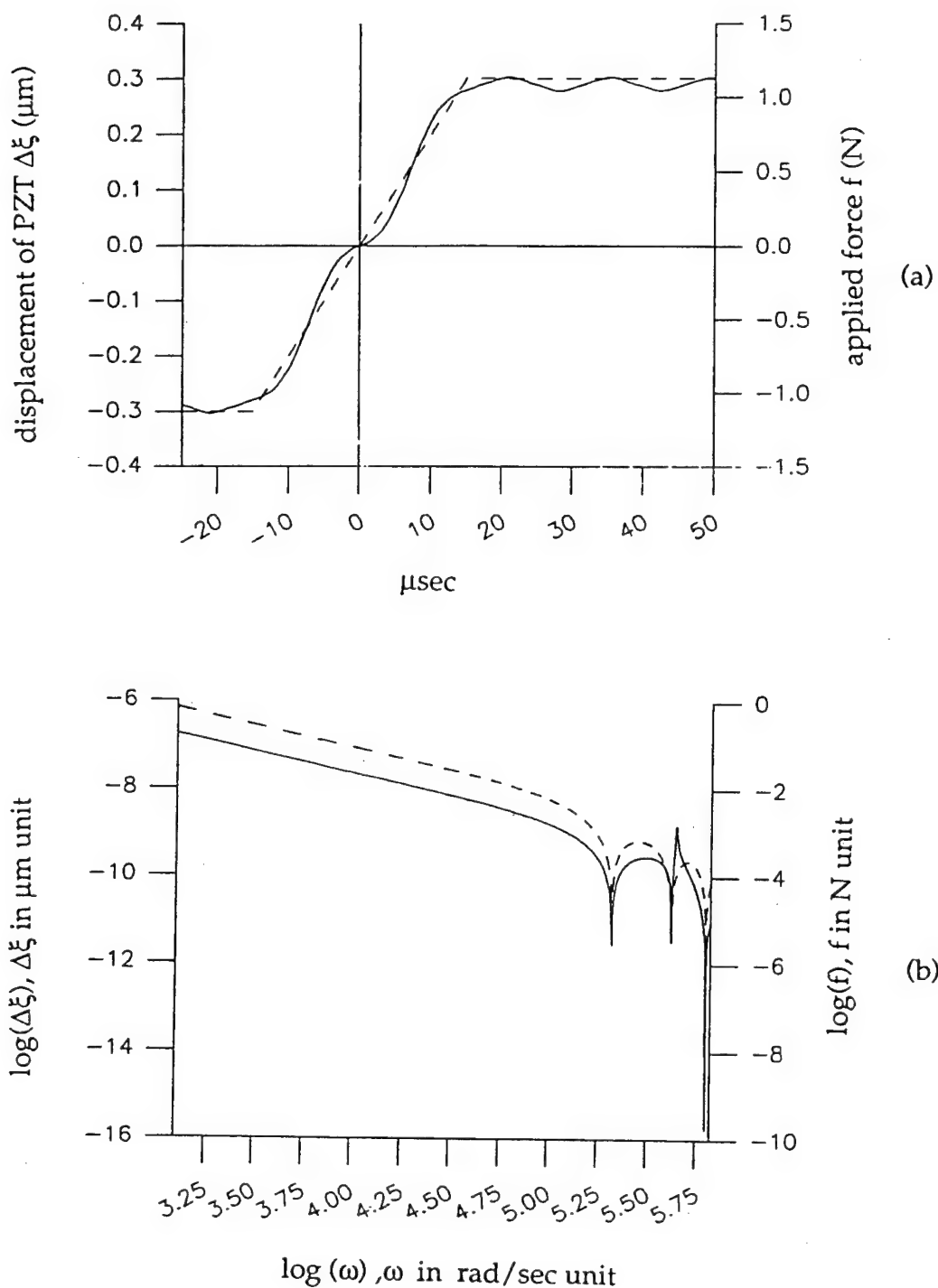


Fig. 18. The simulations with 30 μsec charging time and $\eta = 0.015$. (a) Time domain response. (b) Frequency domain response. In both cases - - - is the applied force, — is the response of the PZT.

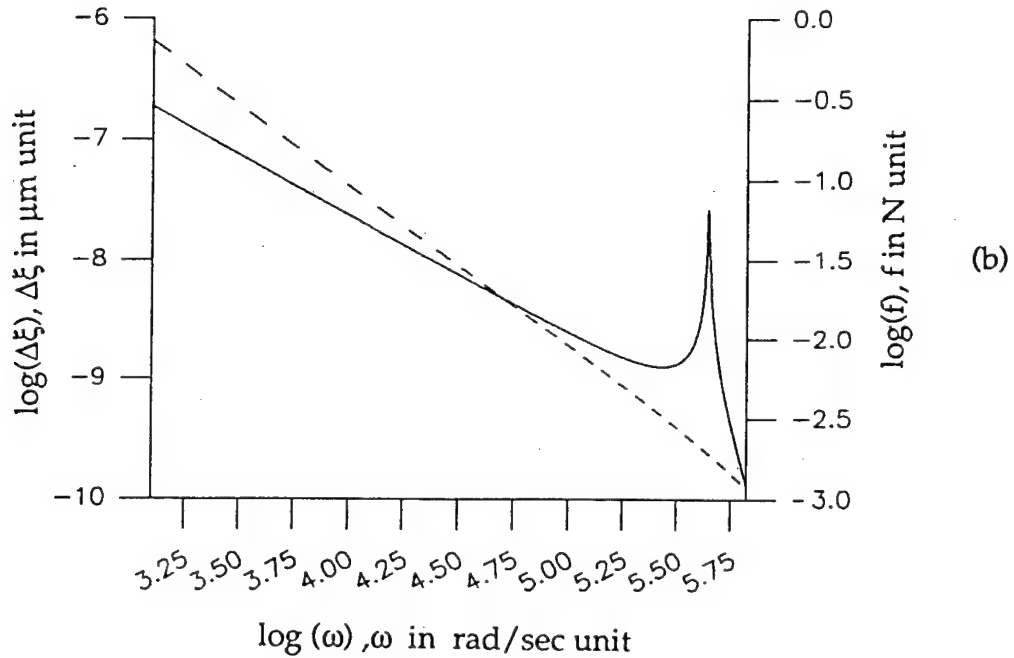
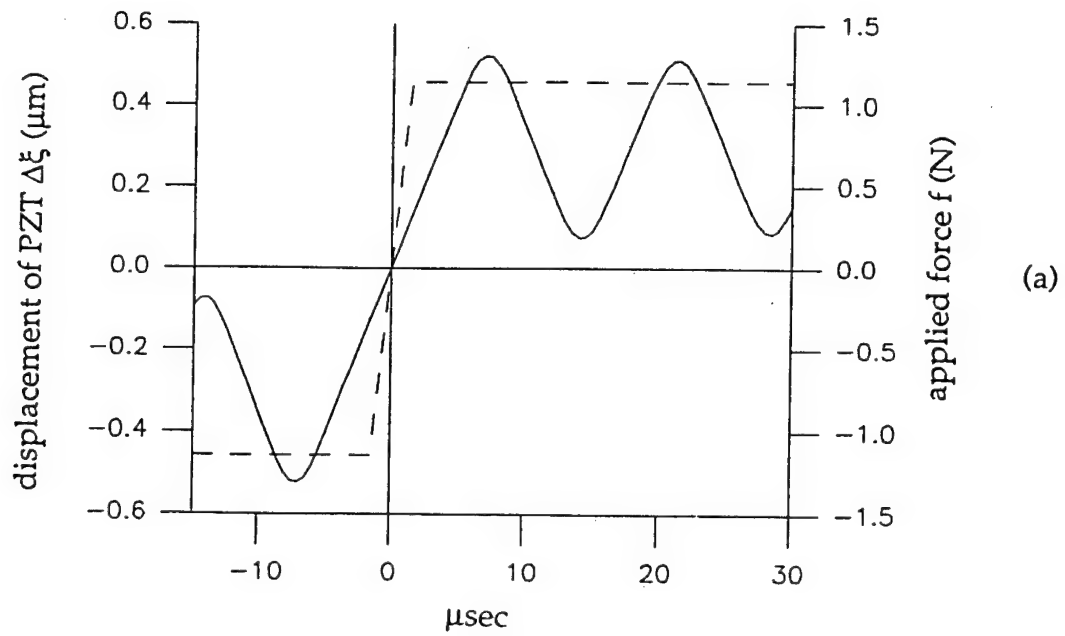


Fig. 19. The simulations with 3 μsec charging time and $\eta = 0.015$. (a) Time domain response. (b) Frequency domain response. In both cases - - is the applied force, — is the response of the PZT.

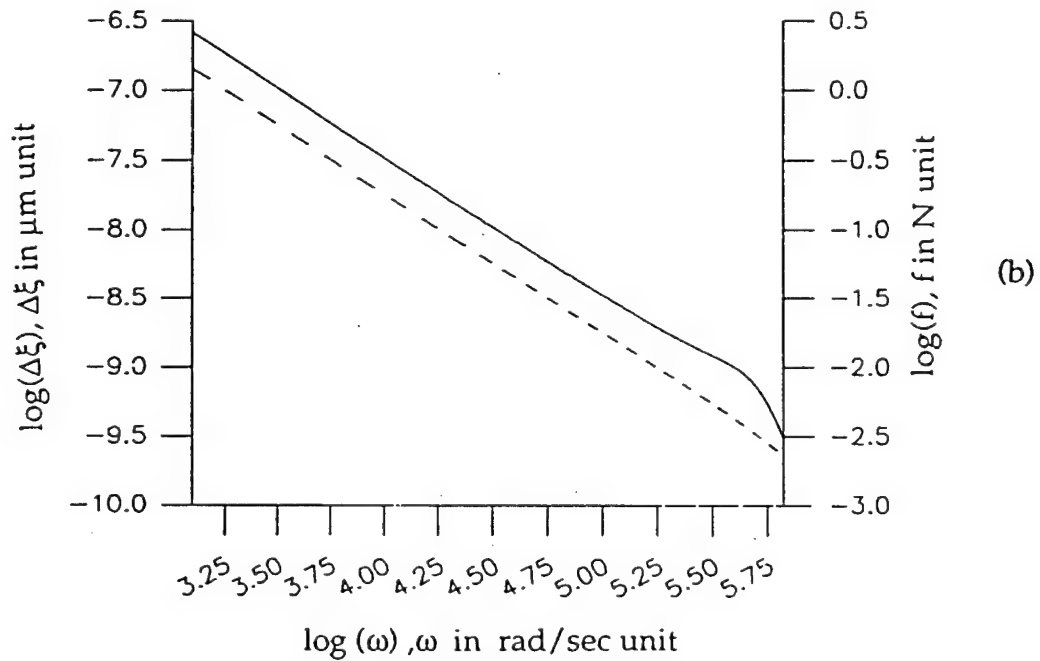
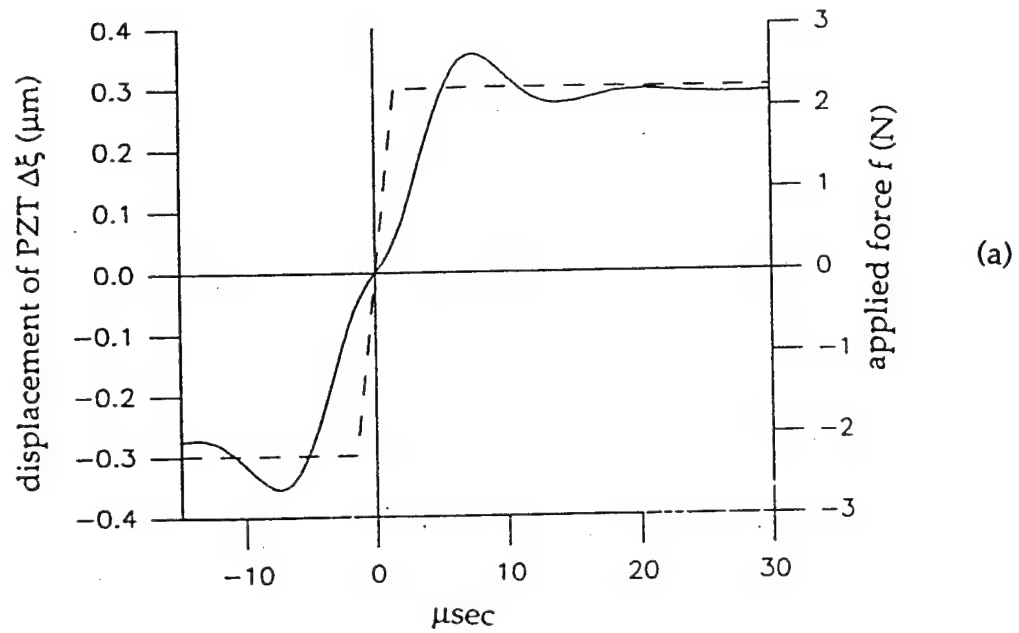


Fig. 20. The simulations with 3 μsec charging time and $\eta = 1.0$. (a) Time domain response. (b) Frequency domain response. In both cases - - - is the applied force, — is the response of the PZT.

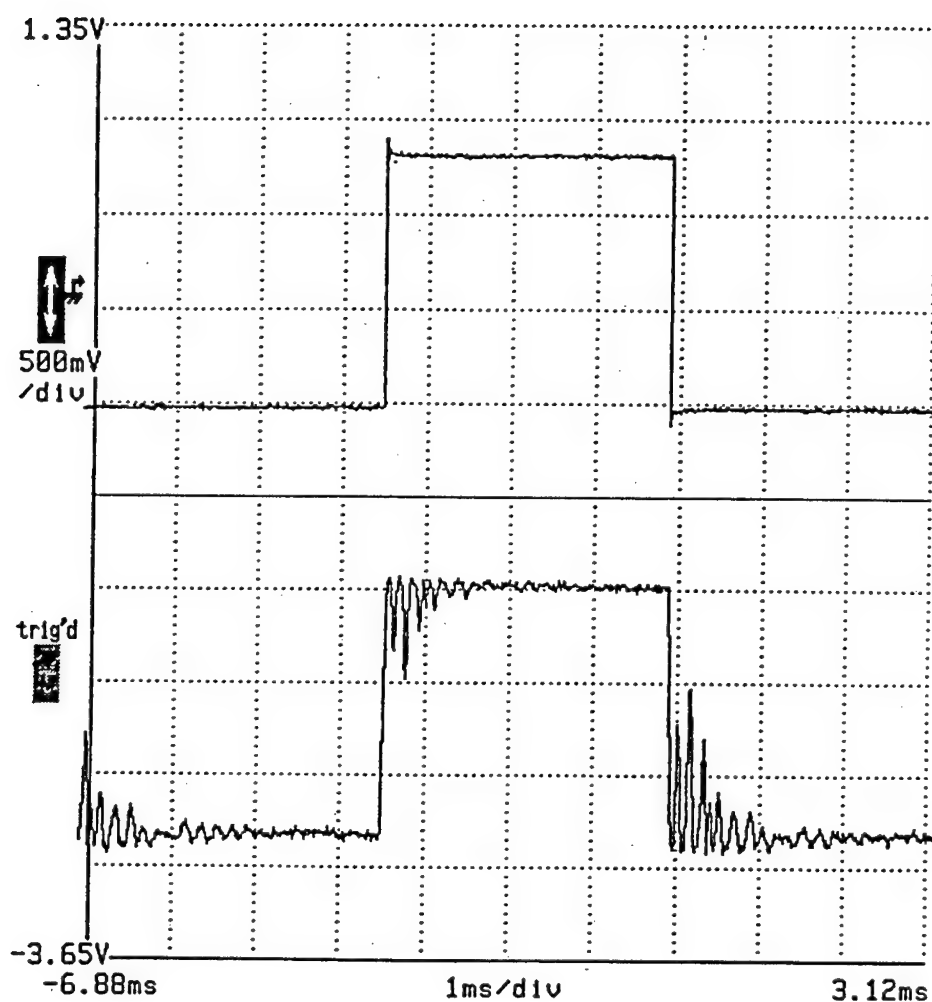


Fig. 21. The switching with 3 μ sec charging time and damping oil (insufficient damping). The upper trace is the voltage across the piezoelectric strips and the lower trace is the optical output from the port of the switch.

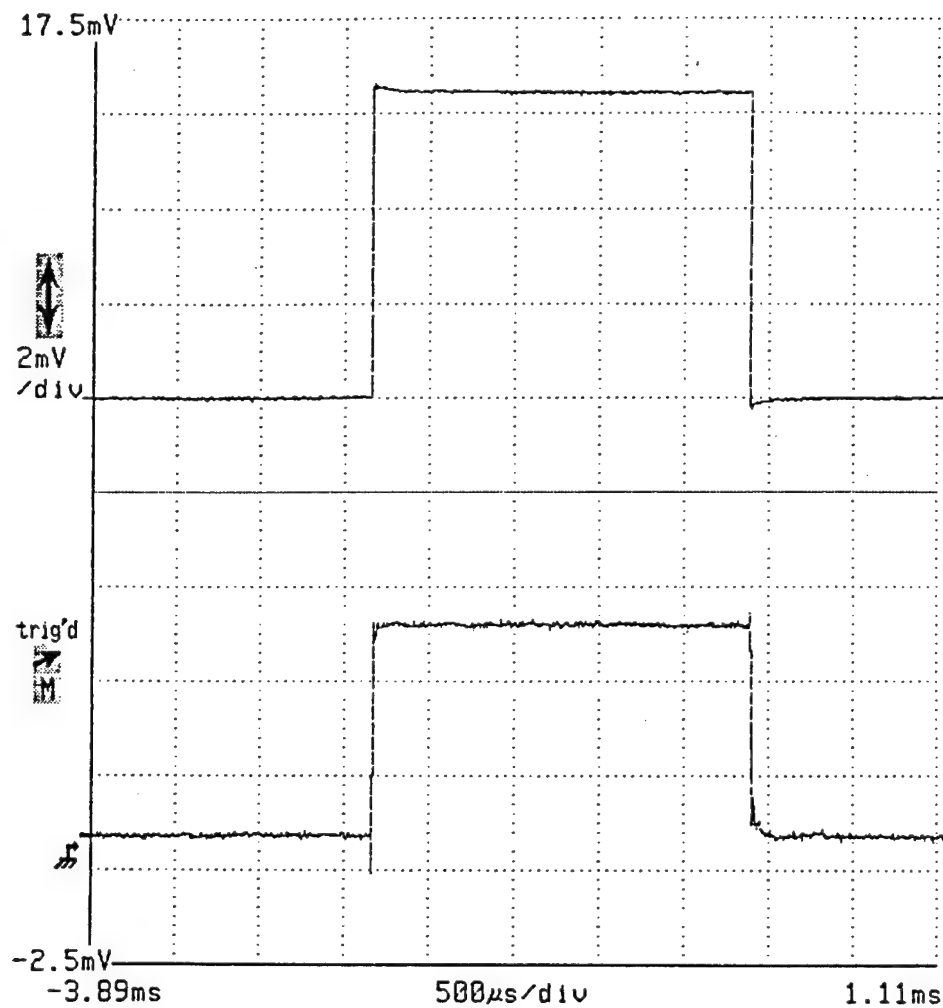


Fig. 22. The switching with 3 μ sec charging time and silicone glue as damping material (strong damping). The upper trace is the voltage across the piezoelectric strips and the lower trace is the optical output from the port of the switch.

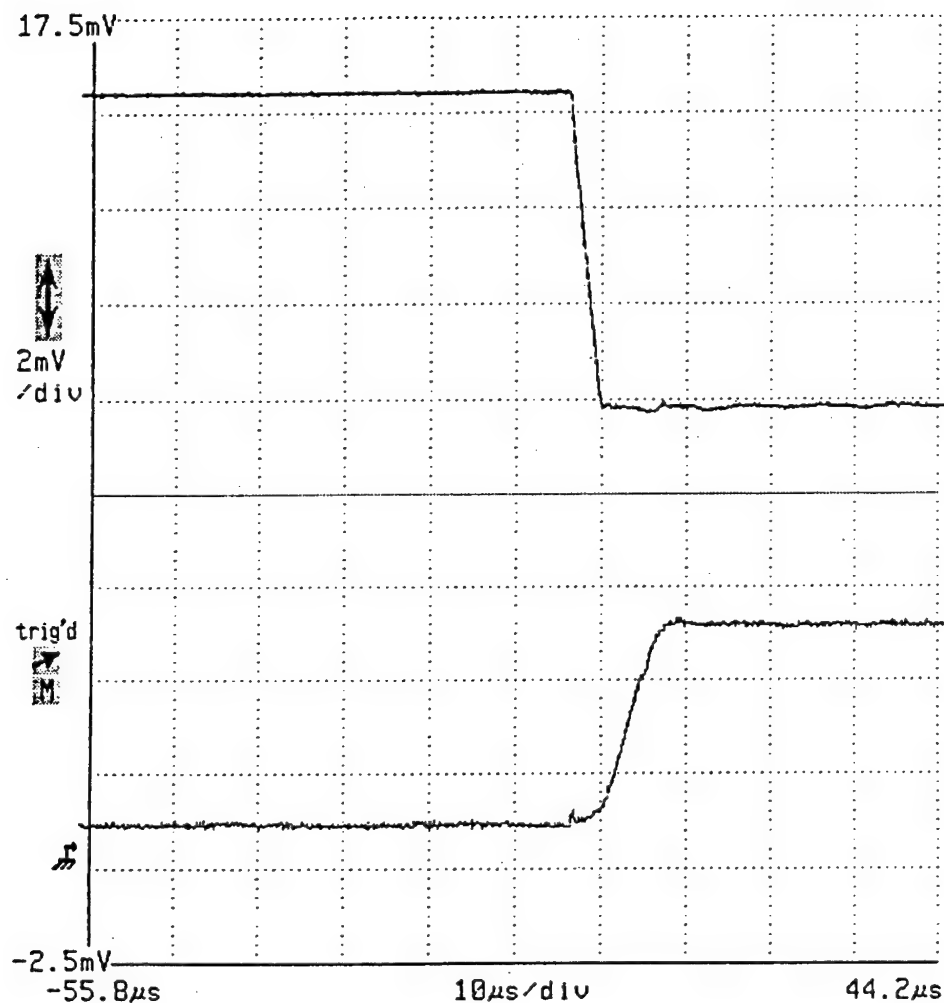


Fig. 23. 8 μ sec switching time with 3 μ sec charging time and silicone glue as damping material (strong damping). The upper trace is the voltage across the piezoelectric strips and the lower trace is the optical output from the port of the switch.

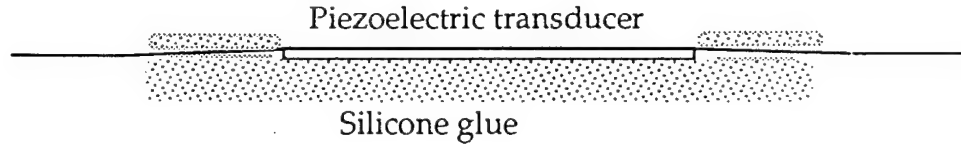


Fig. 24. Silicone Glue used as a Damping Material

where λ is the vacuum wavelength, n is the unperturbed effective refractive index of the fiber, and l is the unperturbed length of the stretched fiber. The change in the refractive index can be written in terms of the strain by using the contracted photoelastic tensor elements p_{11} and p_{12} [17]

$$\Delta n = -\frac{n^3}{2}[p_{12} - \sigma(p_{11} + p_{12})]\frac{\Delta l}{l} \quad (17)$$

where σ is the Poisson ratio and $\Delta l/l$ is the longitudinal strain. The quantity $-\sigma\Delta l/l$ is the transverse strain. Due to the assumed circular symmetry of the fiber, this expression holds for both states of polarization. Combining Eqs. (16) and (17), the phase shift may be expressed in terms of the length change

$$\Delta\Phi = \frac{2\pi n\Delta l}{\lambda} \left\{ 1 - \frac{n^2}{2}[(1-\sigma)p_{12} - \sigma p_{11}] \right\} \quad (18)$$

using the parameter values, $n=1.46$, $p_{11}=0.12$, $p_{12}=0.27$, and $\sigma=0.16$, we find that the contribution due to the change in refractive index $(n^2/2)[(1-\sigma)p_{12} - \sigma p_{11}] = 0.22$ is smaller than, but not insignificant in comparison to, the contribution due to the direct length change.

To change the state of the switch, the applied voltage must alter the relative path lengths of the interferometer arms by π radians. Minimum switching voltage is achieved by attaching PZT elements to both arms of the interferometer, and connecting them so that the applied electric field in one is in the direction of the poling axis and in the other is opposite to the poling axis. This results in expansion of the fiber in one arm of the interferometer, and contraction of the other - and both effects contribute to the path length change.

The displacement of a plate type piezoelectric transducer due to an applied voltage is

$$\Delta L = \frac{d_{31}VL}{thk} \quad (19)$$

where ΔL is the displacement, d_{31} is the piezoelectric charge constant, V is the applied voltage, and thk is the thickness. Using two 2.5 cm X 1.0 cm X 0.5 mm PZT-4 strips, d_{31} is -122×10^{-12} m/V and $\Delta L = \Delta\xi_{\pi/2} = 0.29 \mu\text{m}$, the calculated voltage needed for a π radian phase shift is 48 V. It is smaller than the observed 57 V of V_{π} shown in Fig. 13. The difference is thought to result from nonlinear piezoelectric transducer response and the mechanical loading of the piezoelectric strip by the fiber.

It is worth noting that the power dissipated in the piezoelectric strip is very small (< 1 mW) due to large volume resistance ($> 10^{10} \Omega \cdot \text{m}$) and small capacitance of the piezoelectric strip. Most of the energy required to operate the switch is consumed by the electronic circuit.

2.4 Insertion Loss

The observed optical insertion loss of switch #1 is 0.25 dB. This low optical insertion loss results from the excellent loss characteristics of the fiber couplers (0.1 dB insertion loss for AOFR S501310A) and fusion splices, and provides a large advantage over integrated optics counterparts, with typical insertion losses > 5dB.

2.5 Stability

Optical phase in optical fiber is very sensitive to environment effects, which is the operation principle of optical fiber phase interferometer sensors [18], [19]. This all-fiber optical switch is also a type of phase interferometer. With the advantages of length match and small separation of the interferometer arms, the crosstalk of switch #3 (10 μm arm length difference) was below -27 dB for two hours with a fixed applied voltage and constant temperature environment around the direction couplers. However, when the temperature changed, the crosstalk was less than -23 dB at different applied voltages needed to operate it as a binary state switch, as shown in Table 3. This implies that the nominal phase difference is strongly temperature dependent.

Fig. 25 is a setup for testing the temperature dependence of relative phase difference of a fiber coupler. The fiber coupler, with 30 μm length difference of the two pigtails, had been removed from its package and buffer. Light reflected from the two pigtail ends interfered in the fusion region and was detected by a photodetector over the temperature range from 25 $^{\circ}\text{C}$ to 70 $^{\circ}\text{C}$. The experiments showed that the relative phase changed with temperature, about π radians for every 15 $^{\circ}\text{C}$, although the measurement repeatability was only fair. It is also found that every

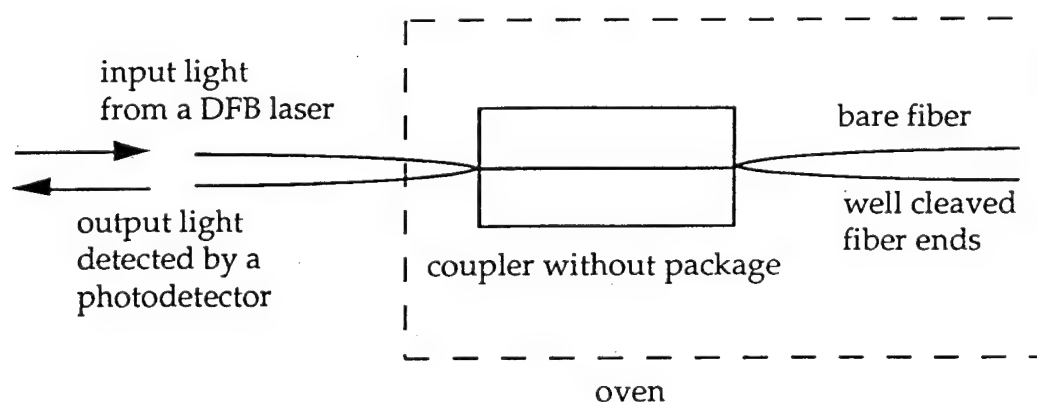


Fig. 25. Measurement of the relative phase difference in a commercial fusion tapered fiber coupler

Table 3. Different applied voltage needed to operate switch #3 as a binary state switch.

Temperature, °C	Applied voltage, V	Extinction ratio, dB
22.2	30.4	-25.8
26.7	46.7	-25.9
30.9	53.7	-25.6
36.6	-28.0	-24.3
41.2	-14.7	-24.3
45.3	-39.2	-24.6
49.0	-25.4	-24.9
53.5	27.4	-23.1
60.3	10.9	-23.8
65.5	28.3	-25.1
70.9	-29.2	-25.2
75.3	-27.6	-25.3
80.4	-20.2	-25.2

fiber coupler had its unique relative phase-temperature relation. The $\pi/2$ phase difference comes from energy conservation of coupling mode theory. Provided that optical loss is accounted, the phase difference does not deviate from $\pi/2$ too much and is not strongly temperature dependent [20]. The coupling ratio variation for incident polarization of the fiber couplers is within 1 %, corresponding to approximately 1° variation of the relative phase difference by coupling mode theory [6]. The diameter of the fusion region in commercial fused-taper fiber coupler is about 30 μm , very small compared to 2 X 125 μm diameter of two optical fibers, moreover the fusion region is fragile. In [21], a 10 μm crack was found in the fusion region of a commercial fiber coupler resulting from humidity and fatigue due to thermal cycling. The formation of the crack can disturb the relative phase difference drastically in the fused-taper fiber coupler. Commercial fiber couplers aim at power splitting stability, instead of relative phase stability. Thus, it is concluded that some property of the fusion region inherent in the fabrication process is the main factor which disturbs the thermal stability of the relative phase difference in the fiber coupler, and ultimately contributes to thermal instability in the interferometer switch.

3. PROGRAMMABLE FIBER-OPTIC DELAY LINE

Fiber-optic delay lines are very useful in signal processing and high-speed communications [22], [23]. The use of optical fiber as a delay medium for signal processing applications was proposed by Wilner and van den Heuvel [1], who noted that fiber delay lines were attractive due to their low loss, low dispersion and high time-bandwidth (TB) product. The time-bandwidth product of single mode fibers is greater than 1,000,000. If the fiber is used for binary data storage, the number of bits is approximately equal to the TB product. A silica fiber provides 5 μs of delay per kilometer of length, so that a long single-mode fiber can store giga-hertz signals for time periods of hundreds of microseconds. This project is devoted to the programmable fiber-optic delay line illustrated in Fig. 2.

3.1 Algorithm and Architecture

The delay time is a function of all the optical switch states and the architecture of the delay lines and switches. In each stage of the delay line, the light is switched through either a short fiber or a longer fiber. In each case, the delay difference is an integer multiple of a unit time delay T . Total delay is the sum of the delays for the individual stages. With m stages, the delay can be varied in units of T from 0 to $(2^m - 1) T$ in units of T , for a total of 2^m different delay times.

Illustrated in Fig. 26, the delay time is changed from 0 to 12 T when the state of switch #2 is changed and others unchanged. Using the other input port with the same action, the delay time is changed from 15 T to 3 T , as shown in Fig. 27.

Consider the case with input port #1. For a time delay of $N T$, N can be decomposed as

$$N = T_0 X 2^0 + T_1 X 2^1 + T_2 X 2^2 + T_3 X 2^3 \quad (20)$$

where T_i is either 1 or 0, which means the light is routed through a long or short fiber.

Take the 12 unit time delay with input port #1 for example, $12 = 0 X 2^0 + 0 X 2^1 + 1 X 2^2 + 1 X 2^3$. Therefore, the switching states from #0 to #3 are straight through, straight through, crossover, and straight through, as illustrated in Fig. 26.

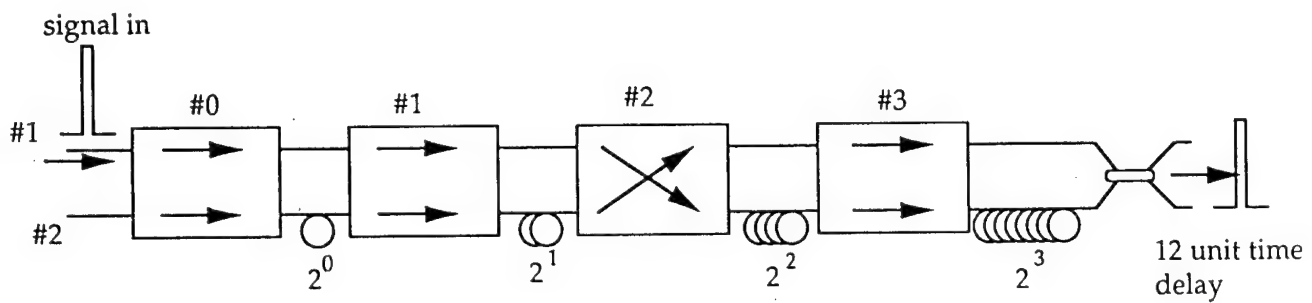
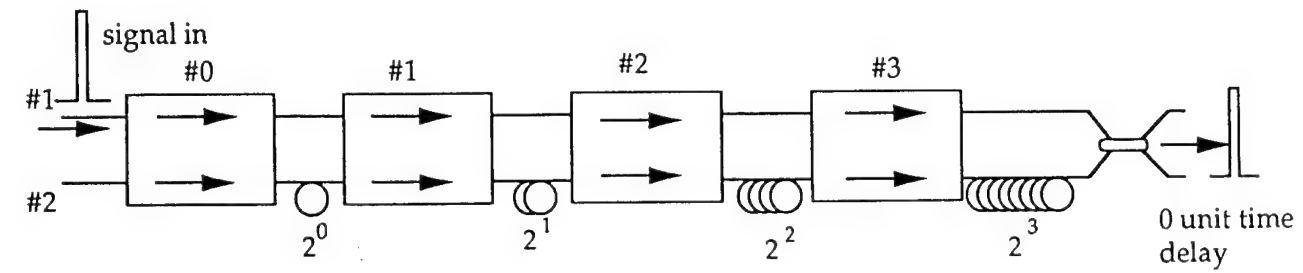


Fig. 26. Delay time changed from 0 to 12 unit time with input port #1 and action of switch #2.

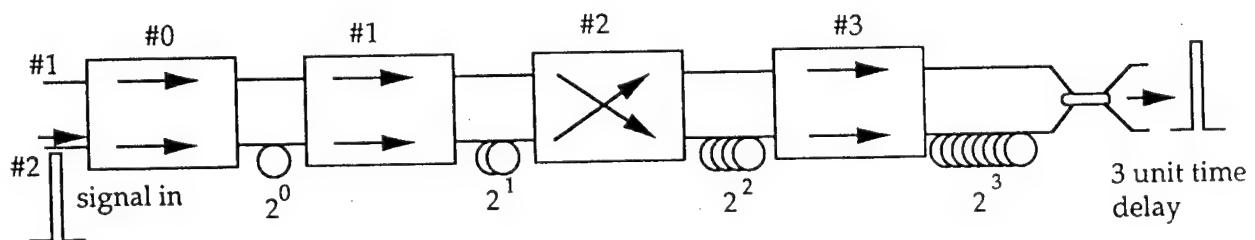
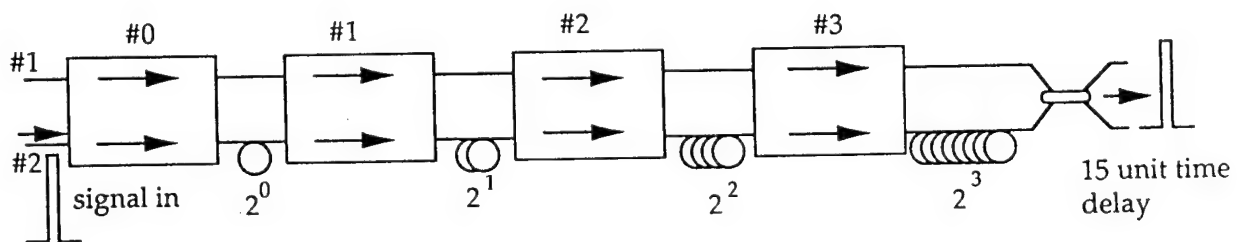


Fig. 27. Delay time changed from 15 to 3 unit time with input port #2 and action of switch #2.

If the input port is #2, then the routing is opposite to that with the input port #1. For the 9 unit time delay with input port #3, $9 = 1 \times 2^0 + 0 \times 2^1 + 0 \times 2^2 + 1 \times 2^3$. Thus, the switching states from #0 to #3 are straight through, crossover, straight through, and crossover.

The 16 time delays with their corresponding switch states and input ports are summarized in Table 4.

3.2 System Performance

The delay line illustrated in Fig. 2 was composed of four piezoelectrically controlled Mach-Zehnder switches with crosstalk less than -22 dB, optical fibers of length of 2 m, 4 m, 8 m, and 16 m, and one 2X2 directional coupler. The system was tested by directly modulating a single mode laser with a pulsed signal (2 nsec width, 250 nsec period) from an Avtech Electro Systems AVM-1-C-0P pulse generator. The output signal was detected by a germanium avalanche photodetector with 30 V reverse bias and displayed on the Tektronix 11201A digitizing oscilloscope.

The 16 different time delays are demonstrated in Fig. 28 by appropriately setting the states of these switches with the algorithm discussed in the previous section. The 16 time delays are 0, 10, 20, ..., and 150 nsec (we regard the signal through the shortest path as zero time delay). The total system loss (the optical power after the 2X2 directional coupler \div the optical power before the first optical switch) was measured to be 4.9 dB, which included 3.1 dB loss of the 2 X 2 directional coupler at the system output. Thus, the loss in the four switch stages was 1.8 db, or 0.45 db per switch stage (0.25 dB from switch and 0.2 dB from fusion splices with delay lines).

A detailed description of experimental procedures and results on the switches and delay line experiments is given in Refs. 30 and 31.

Table 4. The 16 time delays with their corresponding switch states and input ports. S represents straight through; C represents crossover.

switch				input port	
#0	#1	#2	#3	#1	#2
S	S	S	S	0	15
C	C	S	S	1	14
S	C	C	S	2	13
C	S	C	S	3	12
S	S	C	C	4	11
C	C	C	C	5	10
S	C	S	C	6	9
C	S	S	C	7	8
S	S	S	C	8	7
C	C	S	C	9	6
S	C	C	C	10	5
C	S	C	C	11	4
S	S	C	S	12	3
C	C	C	S	13	2
S	C	S	S	14	1
C	S	S	S	15	0
				delay time	

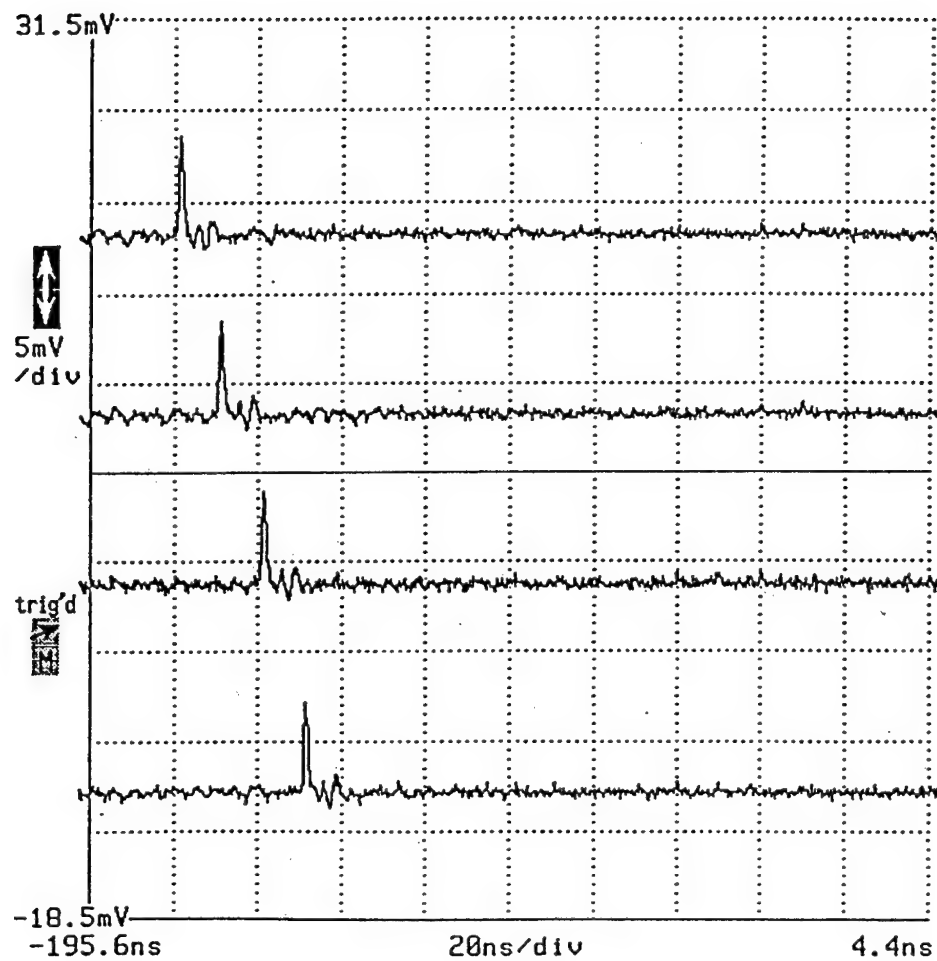


Fig. 28. (a) Results of the programmable optical fiber delay line with time delays of 0, 10, 20, and 30 nano seconds.

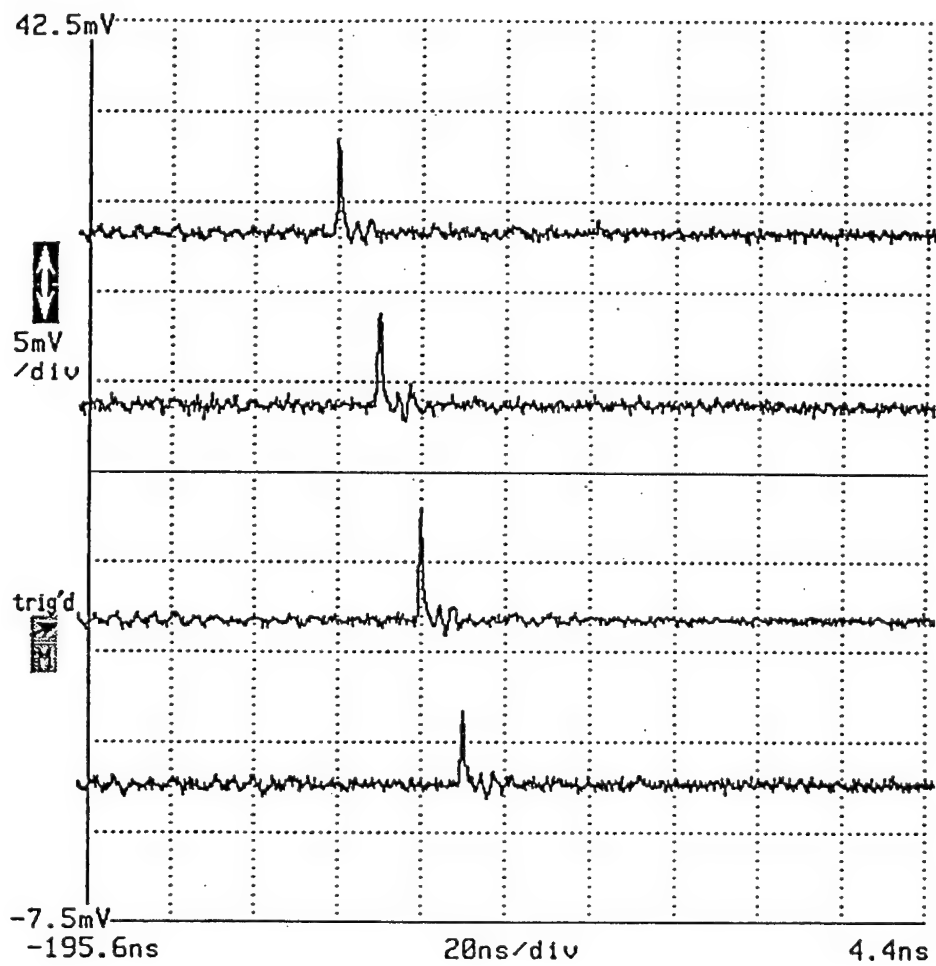


Fig. 28. (b) Results of the programmable optical fiber delay line with time delays of 40, 50, 60, and 70 nano seconds.

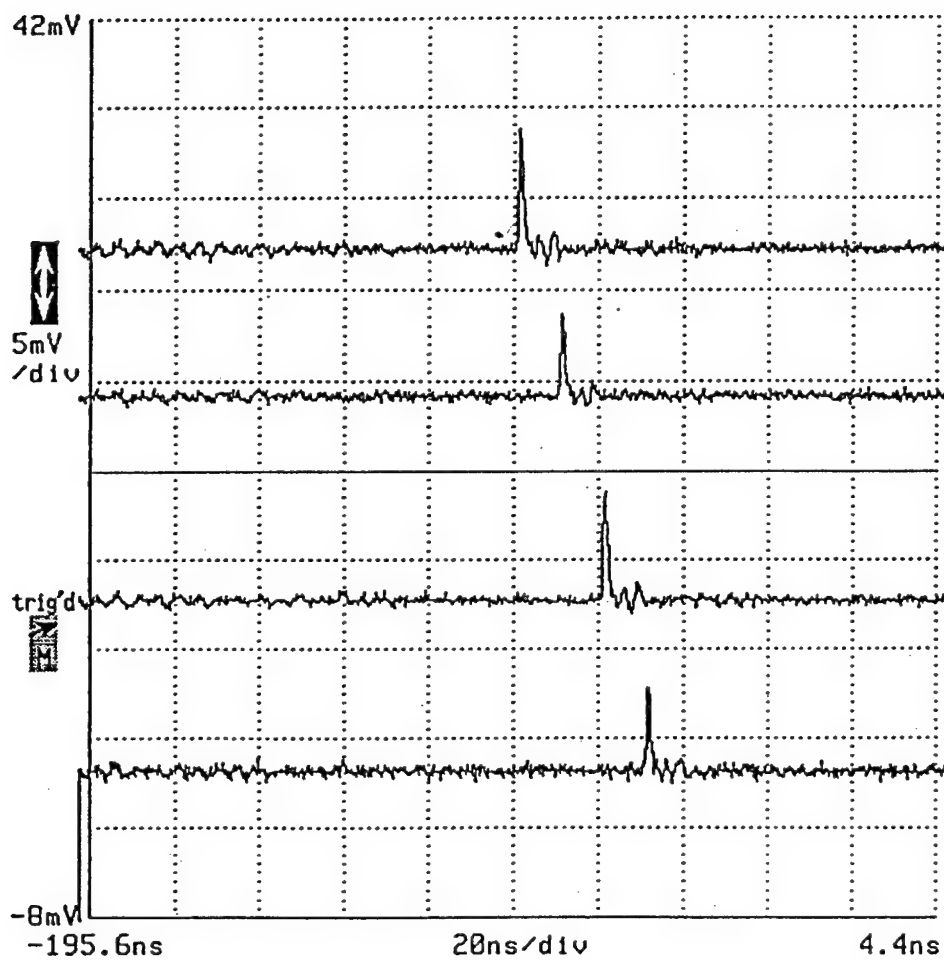


Fig. 28. (c) Results of the programmable optical fiber delay line with time delays of 80, 90, 100, and 110 nano seconds.

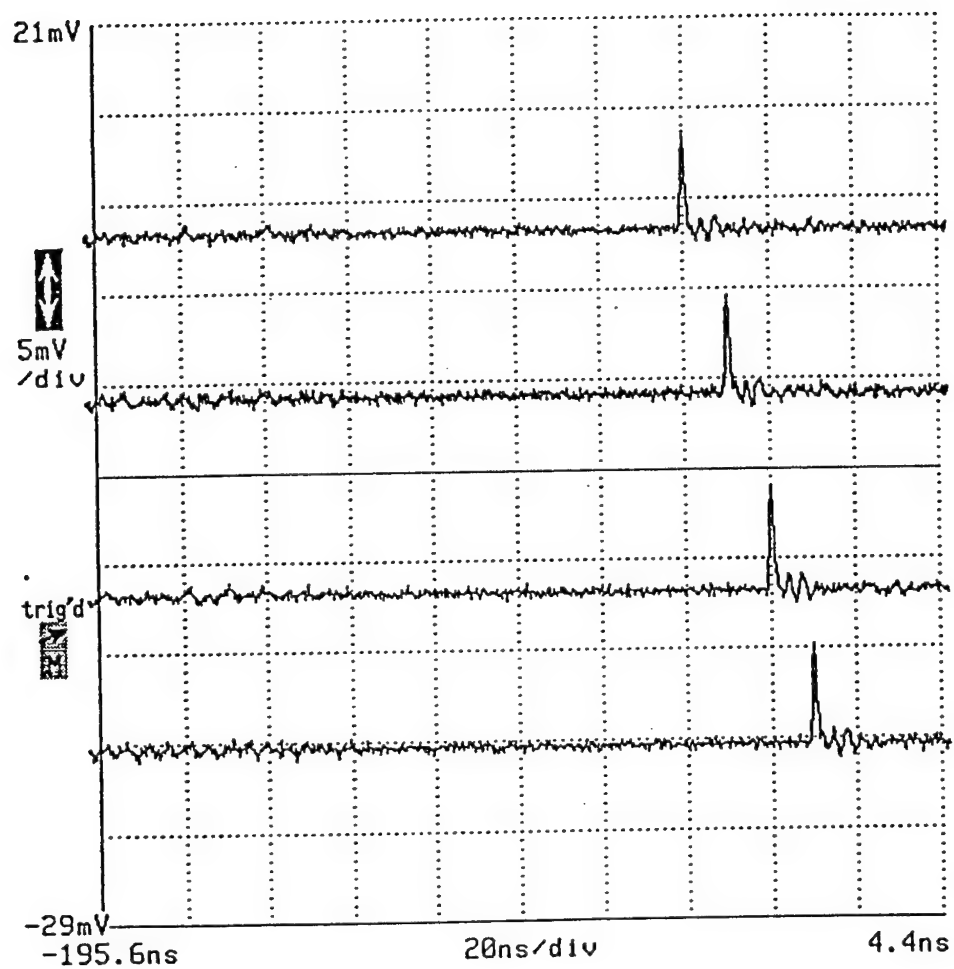


Fig. 28. (d) Results of the programmable optical fiber delay line with time delays of 120, 130, 140, and 150 nano seconds.

4. BROADBAND SEQUENCE GENERATOR

A new method for implementing broadband tapped delay line signal processors has been investigated. The fiber optic processor utilizes N 2×2 optical couplers connected in series to generate and correlate 2^N -bit sequences. The simplest configuration generates and correlates fixed (hard-wired) sequences, but programmable sequences can be implemented by incorporating 2×2 optical switches into the design. Bipolar sequences will be generated by subtracting the outputs from two independent sequence generators operating in parallel, and a correlator design for eliminating spurious correlation peaks will be implemented. Ways to improve the speed of all-fiber 2×2 switches will also be investigated.

The basic configuration for the sequence generator / correlator is illustrated in Fig. 29. A light pulse coupled into an input optical fiber is split into two pulses of approximately equal intensity by a 3 dB optical coupler. The two pulses travel through two fiber sections of different length, corresponding to a time difference of T_1 , and then reach a second 3 dB coupler. The two pulses incident on that coupler are split into four pulses which then traverse two fiber sections of length difference T_2 . This process continues until 2^N pulses reach the $N+1$ 'st coupler. Light passing through that coupler is then converted to an electrical signal by a photodetector.

The time delays differences T_i , $i=1, \dots, N$, are chosen such that each is greater than the input pulse width τ , and no two of the T_i 's are equal. Furthermore, the T_i 's are chosen such that no sum of a subset of T_i 's equals the sum of another subset of the T_i 's, to ensure that 2^N pulses are generated. The first pulse to reach the photodetector is the one which travels through the shortest length of fiber between each pair of couplers. The next pulse to reach the photodetector travels through the shortest interconnecting fibers except for one - the fiber corresponding to the shortest time delay difference T_j ($T_j < T_i$, $i \neq j$). The time of arrival of subsequent pulses is determined by the values of the T_i 's. The last pulse from the sequence generator is delayed relative to the first pulse by a time T_s given by

$$T_s = \sum_{i=1}^N T_i.$$

The output pulse sequence is illustrated in Fig. 1 for the case that $T_1 = 3\tau$, $T_2 = 8\tau$, and $T_3 = 20\tau$. In this example, 8 pulses are generated over a time period of $T_s = 31\tau$. Thus, we see that with 11 couplers in sequence we obtain 1024 output pulses, and with 21 couplers, over 1,000,000 pulses are generated for each incident pulse.

It may be necessary or desirable to boost the optical power level of the pulses at the output of the sequence generator by inserting one or more optical amplifiers (either semiconductor or Er:fiber, for example) into the fiber lines at some point between the light source and photodetector.

The sequence generator of Fig. 29 also can be used as a correlator for the sequence it generates. The primary correlation peak occurs at a time T_s relative to the time that the first pulse reaches the output of the correlator. However, secondary peaks are also obtained at times T' which satisfy

$$T' = T_s \pm \sum T_i,$$

where in this case the sum is over any subset of the T_i 's. These secondary peaks can be within a factor of 2 in amplitude of the primary peak. Thus, the device of Fig. 29 used by itself as a sequence generator and correlator has limited utility for signal processing.

However, this problem can be overcome by using two of the sequence generators of Fig. 29 to produce bipolar sequences, and two identical devices to perform the correlation. The bipolar sequence generator is illustrated in Fig. 30. The input pulse is split into two by a fiber coupler, and the two pulses serve as inputs to "+" and "-" sequence generators with delay times T_{i+} and T_{i-} , $i=1, \dots, N$. The optical outputs from the two sequence generators are converted to electrical signals by separate photodetectors, and the photodetector outputs are subtracted using a differential amplifier. The result is a bipolar sequence, illustrated in Fig. 30 for the case that $T_{1+} = 3 \tau$, $T_{2+} = 8 \tau$, $T_{3+} = 20 \tau$, $T_{1-} = 2 \tau$, $T_{2-} = 4 \tau$, and $T_{3-} = 13 \tau$.

Experimental results corresponding to the diagrams of Figs. 29 and 30 are given in Figs. 31 and 32, respectively. In the experiments a 1.3 μm semiconductor laser diode was pulsemodulated to inject 0.6 ns-wide pulses into the delay network.

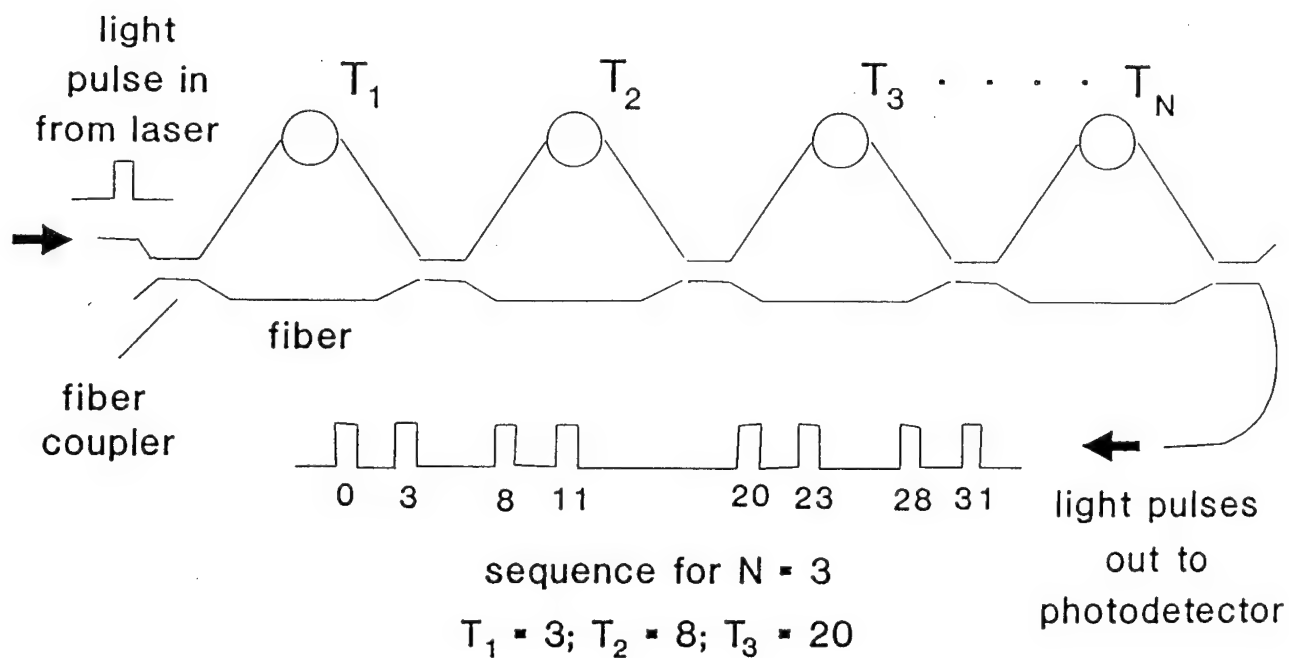


Fig. 29. Configuration for Fiber Optic Sequence Generator

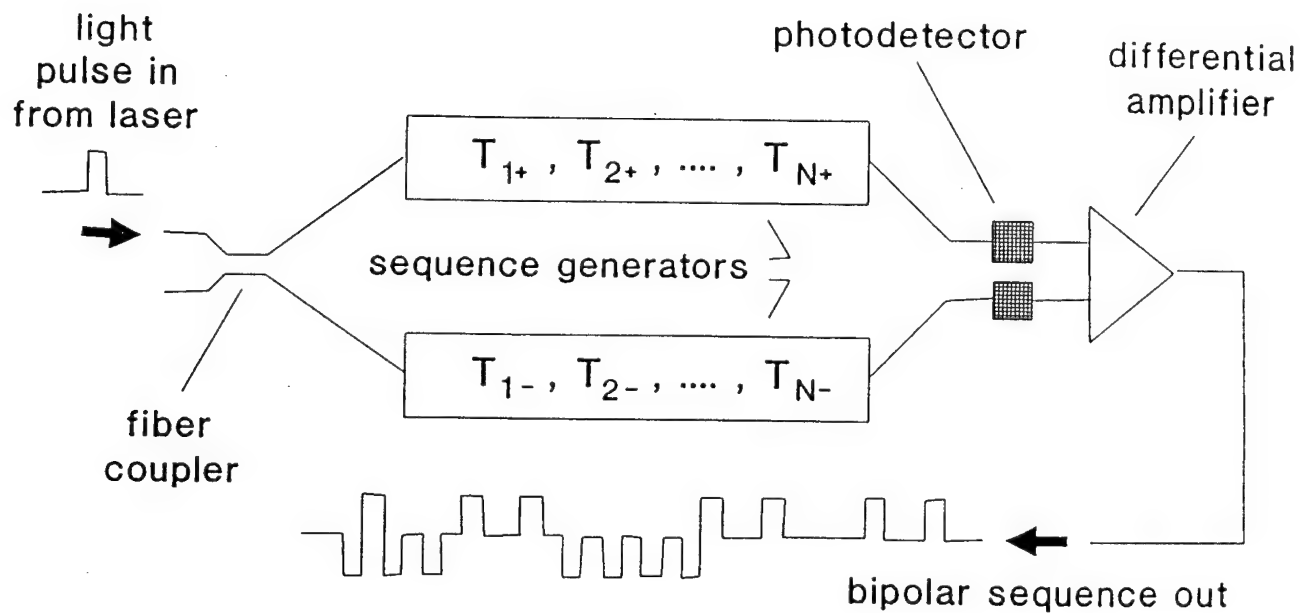


Fig. 30. Configuration for Bipolar Fiber Optic Sequence Generator

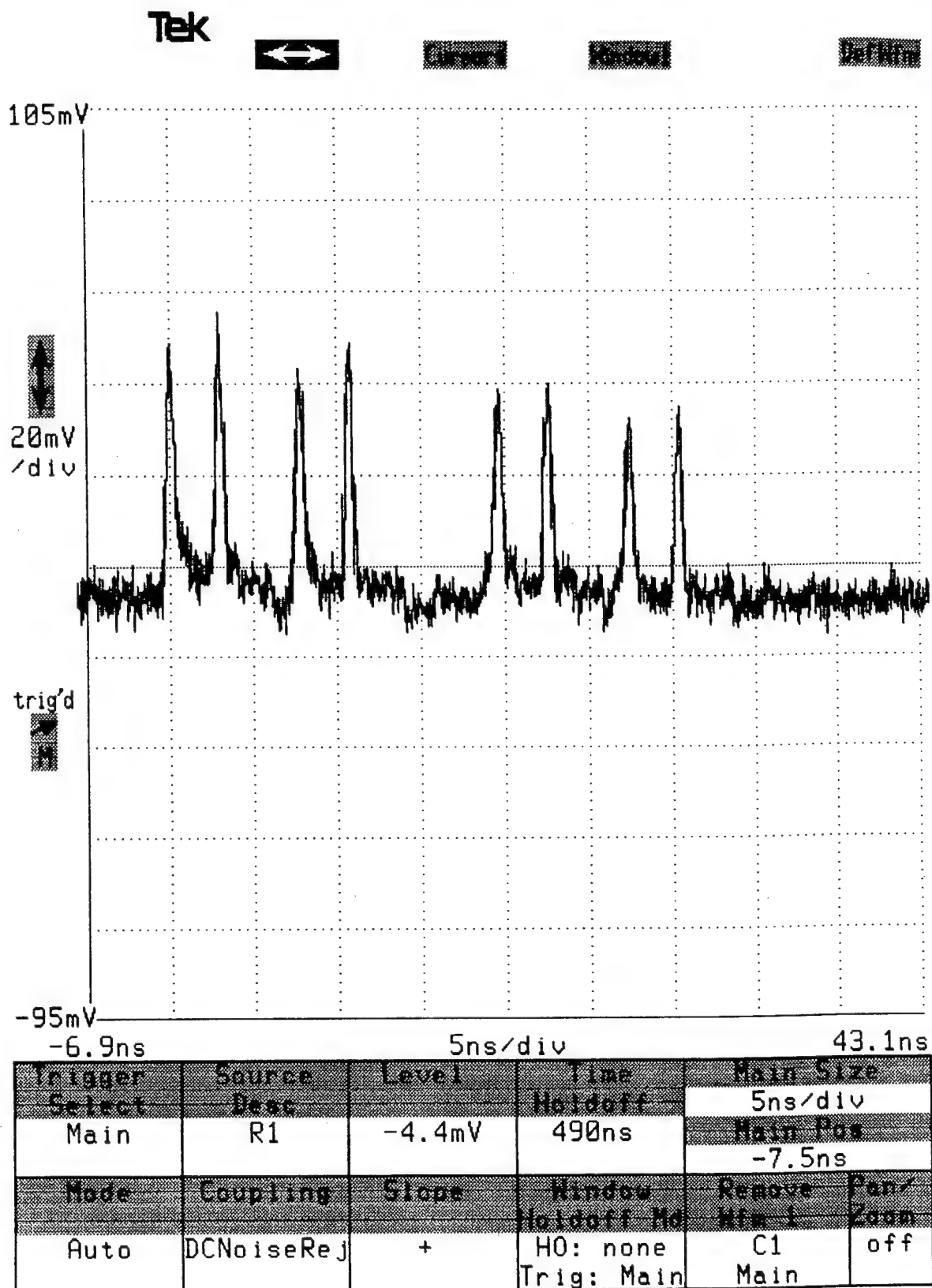
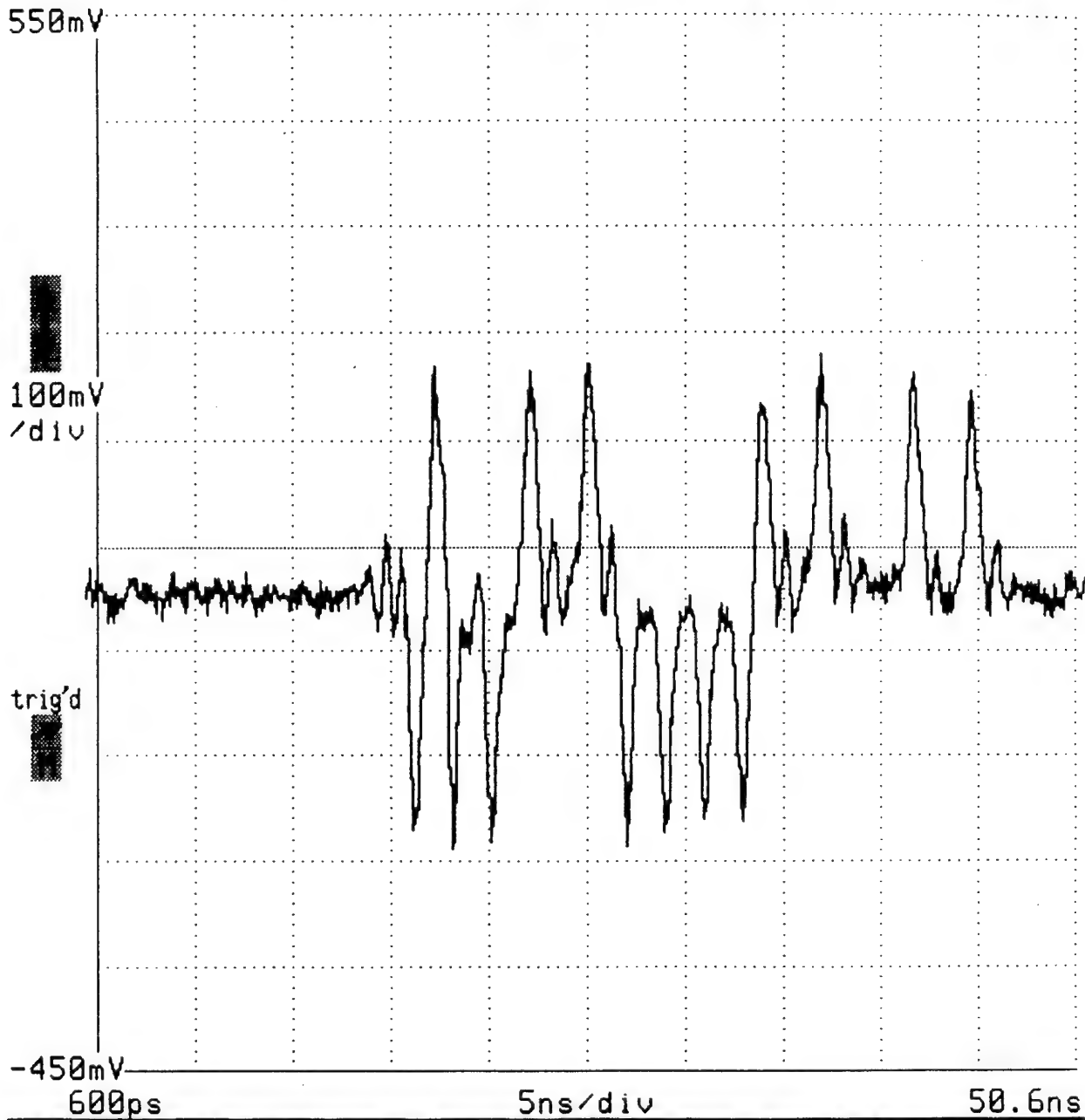


Fig. 31. Experimental Performance of Fiber Optic Sequence Generator

Tek



Vertical	Horizontal	Acquire	Display	Main Size	
Dec	Dec	Dec	Dec	5ns/div	
Avg(C1)	Main	Avg# >8	Linear	Main Pos	
Fast	@ 1024 pts			0s	
Impedance	Coupling	Bandwidth	Page	Source	Page
50Ω	AC	1GHz	All Wfms Status	Avg(C1) Main	off

Fig. 32. Experimental Performance of Bipolar Fiber Optic Sequence Generator

5. DESCRIPTION OF INTRUSION SENSOR SYSTEM

The intrusion sensing system analyzed in this report is intended to detect, locate, and classify intruders over long perimeters [32,33]. One or more fibers contained in a buried cable serve as distributed sensors. Each sensor responds to the pressure of an intruder passing over or near it, as well as to acoustic waves transmitted through the soil from more distant disturbances. Low-flying aircraft might also be detected and located from the acoustic waves they produce. After the presence of an intruder is detected, a signal processor applies a signature analysis algorithm to the raw sensor data to distinguish between people, animals, vehicles, and aircraft. An alternative deployment is to bury the sensor cable under the bed of a lake or river or under the ocean floor to detect boat traffic or swimmers.

Fig. 33 illustrates system deployment and the presentation of processed sensor information to users. A monitoring site at one end of the sensing cable contains optical and electronic components, including a laser, a photodetector, and a signal processor. The raw sensor data is processed to determine the location and classification of each intruder, and this information is displayed in user-friendly fashion. A zoom feature is provided for high-spatial-resolution display of intruder activity over a portion of the perimeter being monitored.

The distributed intrusion sensor proposed here is configured as a coherent optical time-domain reflectometer (coherent OTDR). Conventional (non-coherent) OTDR equipment is widely used in the telecommunications industry to locate breaks in fiber optic cables. A schematic illustration of a conventional OTDR system is shown in Fig. 34. In such a system, light pulses from a semiconductor laser are injected into one end of the fiber, and the light returned from the fiber as a result of Rayleigh backscattering is monitored with a photodetector. Rayleigh scattering is a phenomenon in which inhomogeneities frozen into the fiber when it cools during drawing act as a microscopic scattering centers, as in Fig. 35. The light is scattered in all directions from these centers, but only that scattered in the backward direction and captured in the core of the fiber is detected by the OTDR. Discontinuities in the plot of reflected power vs. time indicate the presence and location of breaks or localized sources of attenuation in the fiber. However, conventional OTDR is not nearly sensitive enough to either pressure or acoustic waves to be used in intrusion sensing. An optically coherent OTDR which makes use of interference between light waves backscattered or reflected from different parts of the fiber will be needed to achieve the required sensitivity.

The baseline design for the coherent OTDR intrusion sensor is illustrated schematically in Fig. 36. Both buried and underwater deployment of the distributed sensor are possible. For underground deployment, we envision a small (≈ 2.5 mm or 0.1" diameter) fiber cable buried 30 to 60 cm (1' to 2') beneath the surface. The fiber acts as a pressure sensor; that is, the pressure from the weight of the intruder on the surface of the soil near the sensor causes a change in the phase of the optical carrier propagating in the fiber. The fiber also is sensitive to acoustic waves transmitted through the soil. As with conventional OTDRs, light pulses from a laser are injected into one end of the fiber, and the returned light from the fiber is monitored with a photodetector. The difference in comparison with conventional OTDRs is the high degree of coherence of the light source. The coherent OTDR needs a light source spectral width of the order of 10 - 100 kHz, vs. 1 GHz or more for the conventional OTDR. To achieve the narrow spectral width, the laser is operated continuously and the pulse is gated with an external modulator that is quickly turned on and off. The phase shift in the optical carrier caused by the intruder's presence is

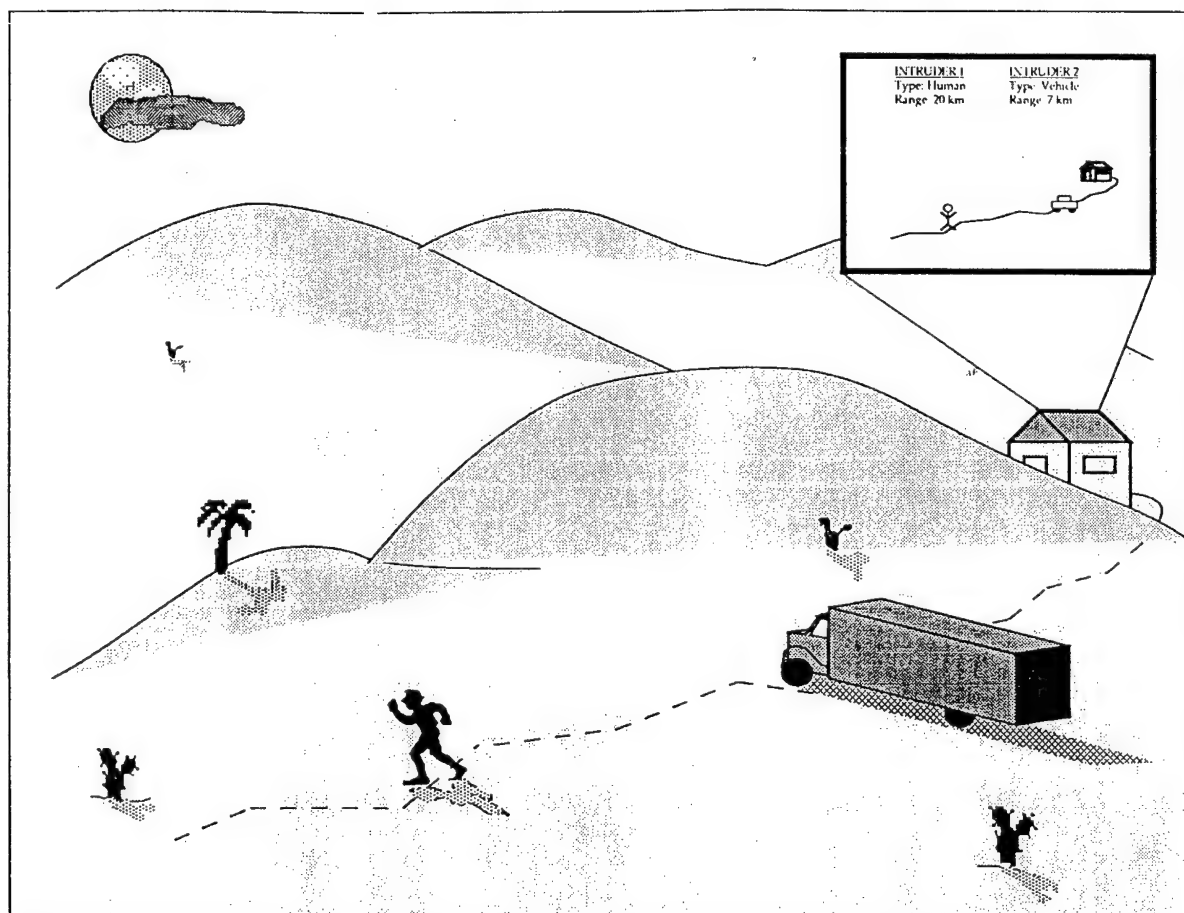


Fig. 33. Configuration for distributed fiber optic intrusion sensor system.

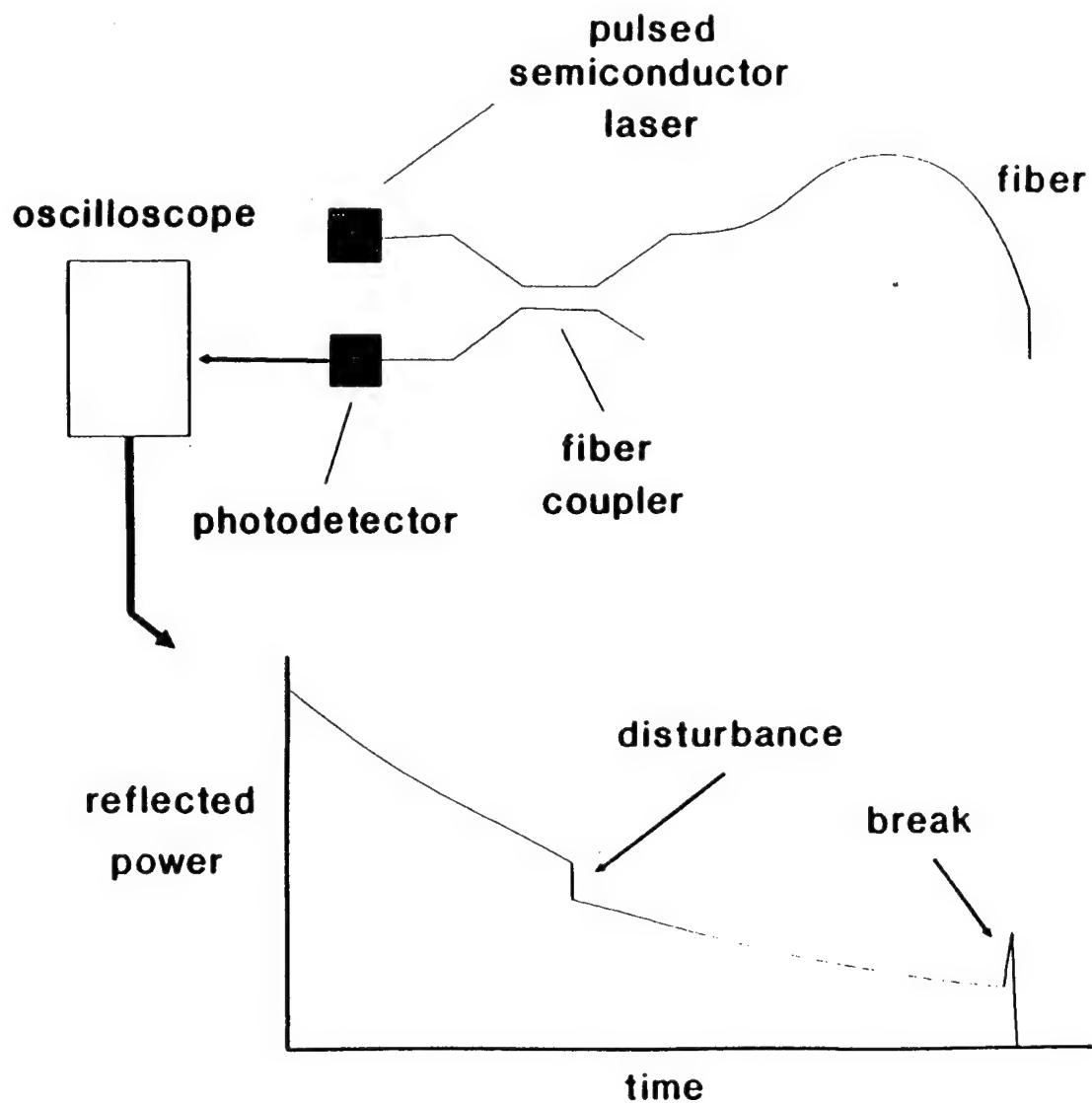


Fig. 34. Conventional OTDR system.

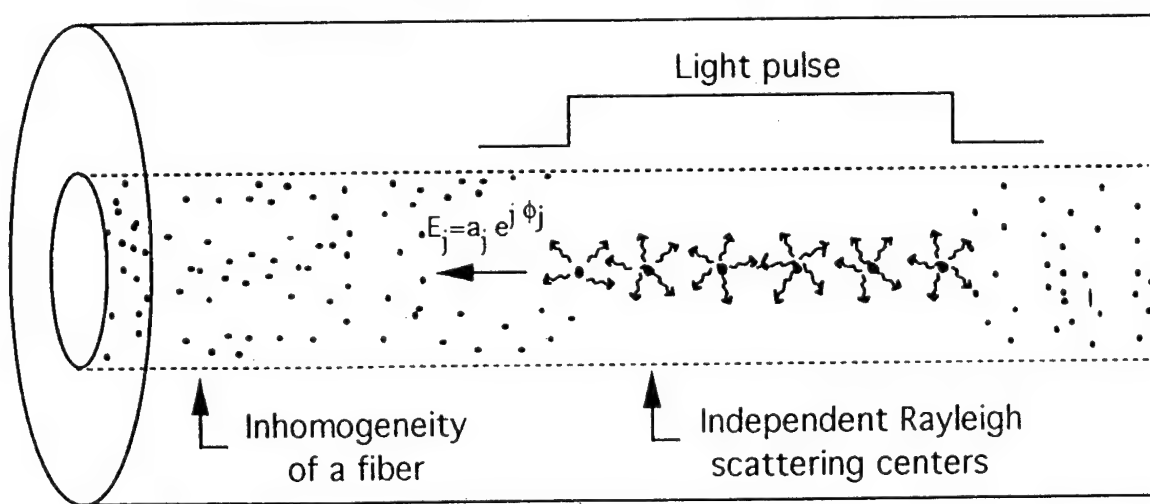


Fig. 35. Schematic illustration of Rayleigh scattering

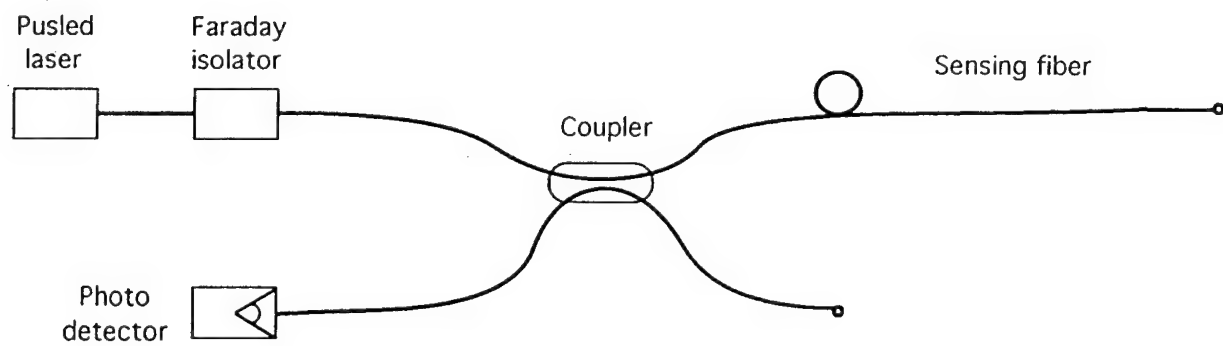


Fig. 36. Coherent OTDR system.

converted to an intensity change by optical interference at the photodetector, in the system illustrated in Fig. 36. The photodetector's analog output signal is digitized and processed in a time-resolved manner, as in pulsed-radar signal processing. A change in the amplitude of the returned signal in a particular time bin indicates the presence of an intruder at the location corresponding to that time bin, as illustrated schematically in Fig. 37. Further processing of the data will minimize false-alarm rates; e. g., by using signature analysis to distinguish human intruders from animals and weather-related phenomena.

During the course of the analysis, it has been determined that modifications to the original system design can give significantly improved detection range (length of the distributed sensor) or range resolution. The first new design involves the use of polarization-resolved detection of the return light from the sensing fiber, as in Fig. 38. In this case, the light is separated into four independent polarization components which are separately detected and processed.

Implementation requires only a modest increase in system complexity and cost over the baseline approach of Fig. 35. The second alternative design makes use of reflecting splices inserted along the length of the fiber, as in Fig. 39. This alternative will require significant modification to the fiber cable.

6. COMPONENT SELECTION FOR INTRUSION SENSOR SYSTEM

Parameter values for commercially available components were used for obtaining numerical results in the analysis of system performance. In making the component selection, the following system parameters were used as guidelines:

TABLE 5. DESIRED SYSTEM PERFORMANCE PARAMETERS

parameter	longer range, lower resolution system	shorter range, higher resolution system
range (km)	20	5
range resolution (m)	100	20
signal frequency range (Hz)	3-300	3-300
cable burial depth (max, cm.)	60	60

The components indicated below are the baseline for the analysis.

Light source. The laser must operate continuously with a very narrow linewidth at a wavelength near a transmission window for low-loss silica fiber (i. e., 1.3 μm or 1.55 μm). The only type of commercial laser which meets these requirements is the Nd:YAG laser pumped by a semiconductor laser (diode-pumped YAG laser). We have selected the Model 123-1319-040-F laser supplied by Lightwave Electronics of Santa Clara, CA, which has the following specifications:

- configuration: non-planar ring
- wavelength: 1.319 μm
- output coupling: single mode fiber, via Faraday isolator
- output power: > 40 mW
- linewidth: < 5 kHz over 1 msec
- frequency drift: < 75 kHz in 1 sec

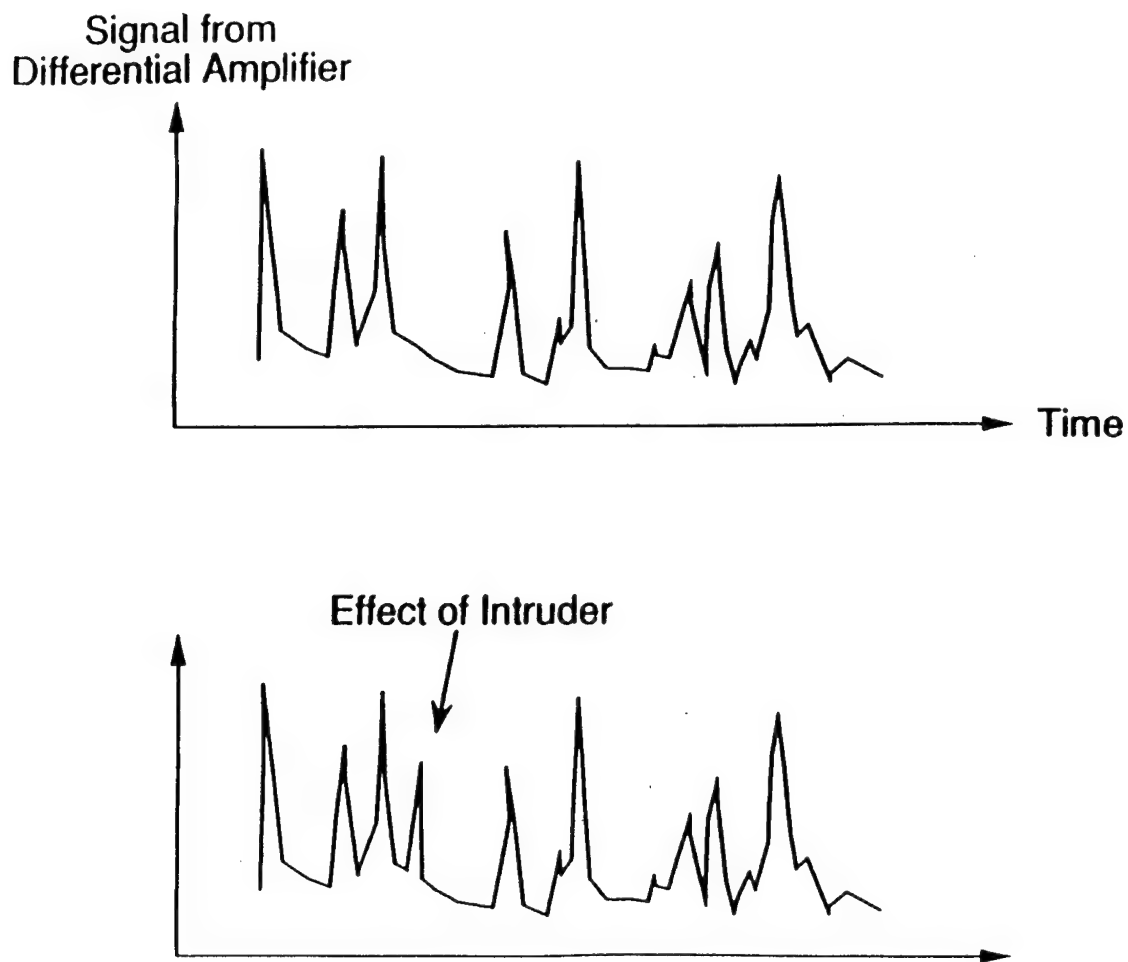


Fig. 37. Response of coherent OTDR to localized phase perturbation in fiber.

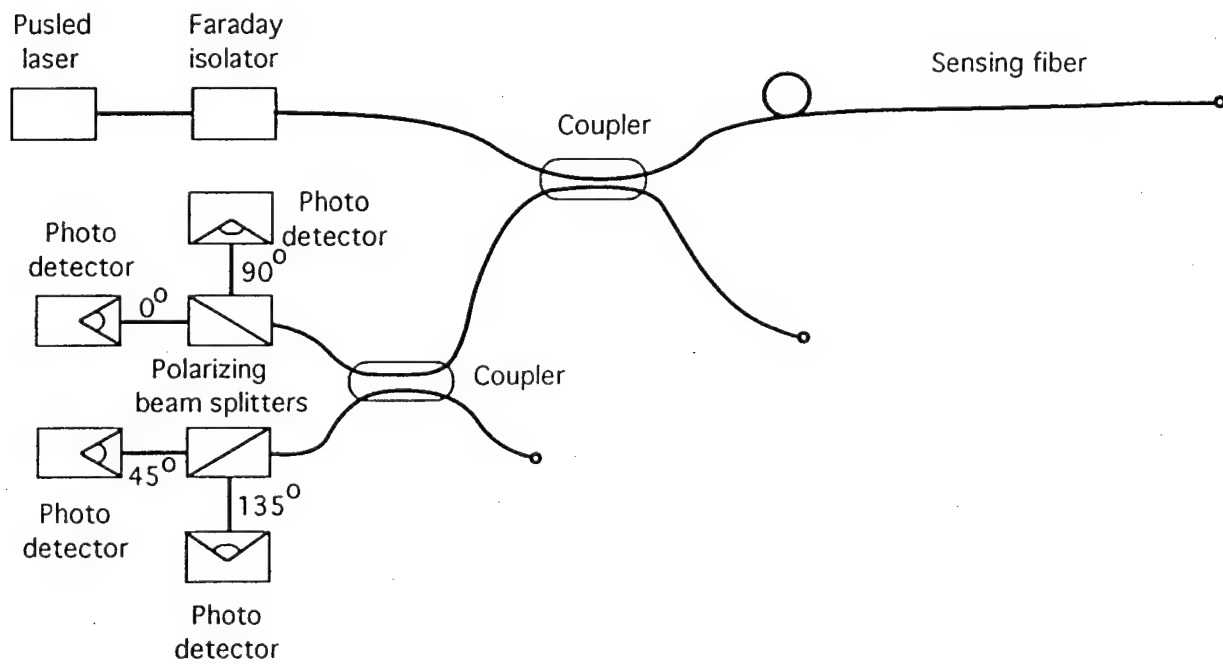


Fig. 38. Coherent OTDR with polarization discrimination.

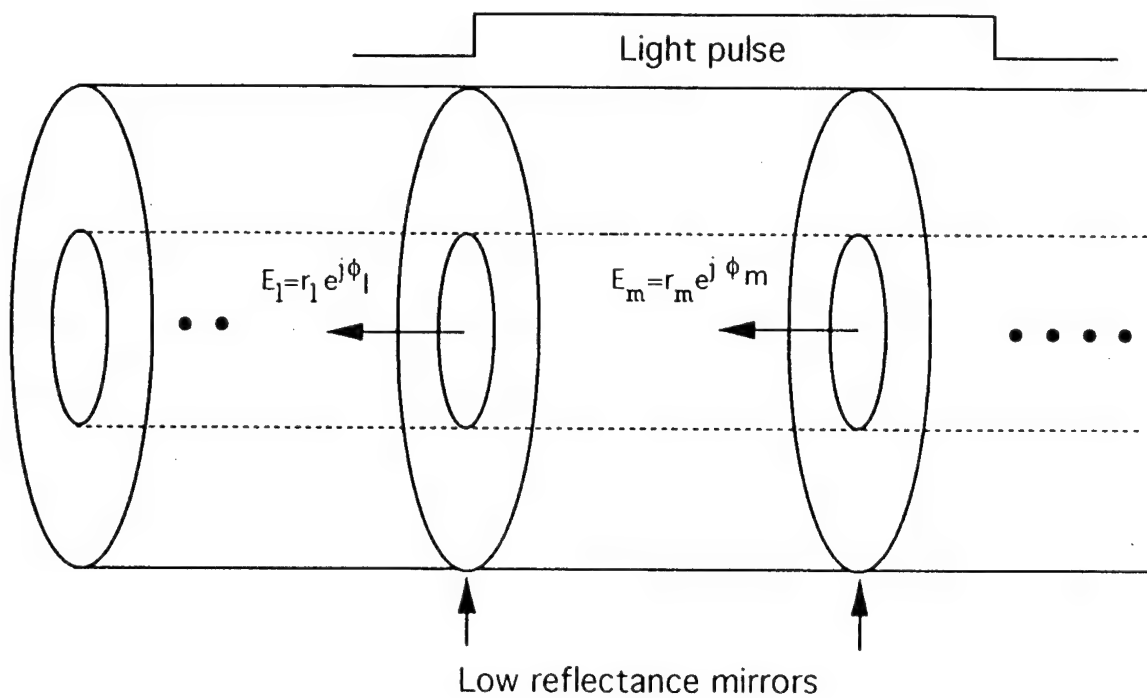


Fig. 39(a). Fiber with reflective splices.

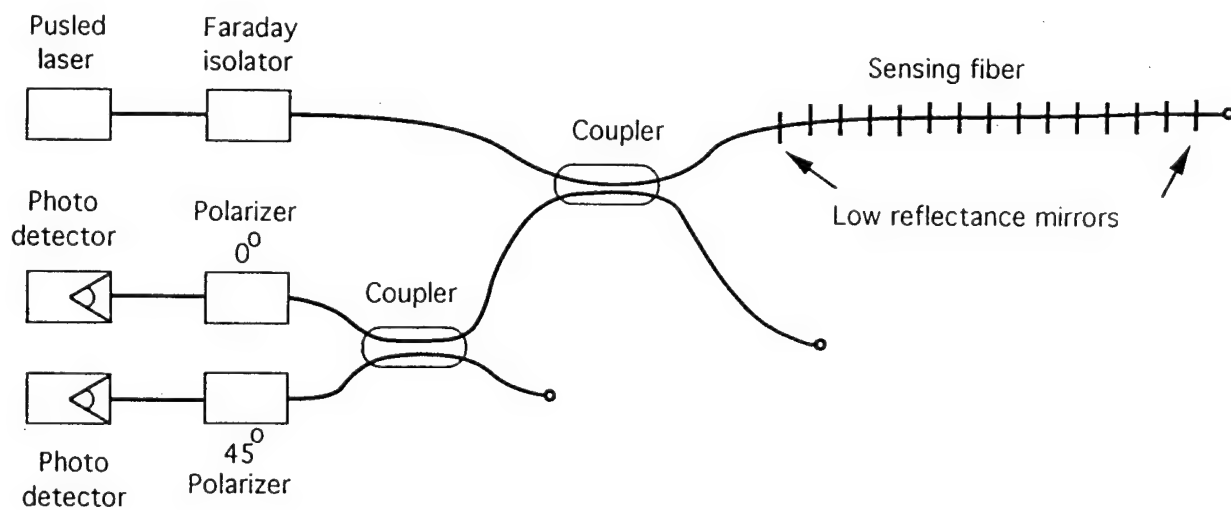


Fig. 39(b). Coherent OTDR using fiber with reflective splices.

fast frequency tuning means: intracavity piezoelectric

frequency tuning response bandwidth: > 100 kHz

In the intrusion sensor system, the laser frequency will be locked to a fiber ring resonator using the piezoelectric element for frequency tuning to reduce the drift to < 5 kHz over 1 sec.

Optical modulator: The optical modulator gates the light from the laser into a single mode fiber to produce a short (100 ns - 1 μ s) pulse of highly coherent light. A suitable modulator is Model m2112AA, an electrooptic device supplied by AT&T Microelectronics, Allentown, PA, which has the following specifications:

input and output coupling: single mode fiber

design wavelength: 1.3 μ m

insertion loss: < 3 dB

modulation bandwidth: > 4.0 GHz

Optical coupler: The optical coupler splits the incident light into equal-amplitude components (50:50 splitting), thus performing the function of a beam splitter in the sensor system. A suitable coupler is Model SMBC-50/50-A-1300-2x2 from Iptek, Carlsbad, CA, which has the following specifications:

input and output coupling: single mode fiber

design wavelength: 1.3 μ m

splitting ratio: 50%/50% $\pm 2\%$

excess loss: < 0.1 dB

Sensor cable: The cable containing the sensing fiber should be small yet rugged and suitable for buried deployment. The single fiber tactical cable Model LTC-1SXS-AX, supplied by AT&T Network Systems, Norcross, GA, is suitable for the intrusion sensor demonstration. It has the following characteristics:

fiber type: single mode

core diameter: 8.8 μ m

cladding diameter: 125 μ m

buffer material: hytrel

tensile strength members: aramid yarn

outer jacket: polyurethane

cable diameter: 2.5 mm

tensile strength: > 270 N

cabled fiber attenuation @ $\lambda = 1.3$ μ m: < 0.4 dB/km

Optical receiver: The optimized optical receiver is very similar to those used in communications, which are designed for minimum noise at low optical signal levels. The desired photodiode characteristics are high quantum efficiency, low capacitance, low dark current, and high bandwidth. The Model NDL5405 photodiode from NEC is suitable for this application.

Characteristics are:

structure: InGaAs PIN

diameter of active area: 80 μ m

quantum efficiency: $> 80\%$

dark current: 0.1 nA (typical)

capacitance: < 1.5 pF

rise time: < 1.0 ns

A transimpedance design will be used for the FET preamplifier. The high bandwidth (≈ 500 MHz) of the photodetector will make it possible to overcome thermal noise by using a large value for the feedback resistor in the preamplifier.

7. SIMULATIONS OF INTRUSION SENSOR SYSTEM PERFORMANCE

In the coherent OTDR of Fig. 36, a light pulse of width τ is coupled into the fiber and the backscattered light is converted to an electrical signal of duration T , where $T = 2L/(n_g c)$, with L the fiber length, n_g the group refractive index for the fiber mode, and c the free-space velocity of light. For a silica fiber, $T = 10L$, with T in μs and L in km. Thus, for a 20 km fiber, the duration of the return signal is 200 μs . The spatial resolution Δz is of the order of $2\tau n_g c$, or $\Delta z \approx 100\tau$, with Δz in m and τ in μs . For a pulse width $\tau = 1 \mu s$, then $\Delta z \approx 100$ m.

The signal processor divides the return signal into time bins of temporal width $\alpha\tau$, with α an adjustable parameter which is typically taken to be in the range between 0.5 and 1.5. Thus, the j 'th time bin contains the accumulation of the charge generated by the photodetector during the time interval $j\alpha\tau < t < (j+1)\alpha\tau$, with the time t measured with respect to the initiation of the laser pulse. The signal processor accumulates the charge in each time bin over N pulses and stores the result as $\{C_j\}_K$, where the j is the index of the time bin and K is the index of the N -pulse average. This process is repeated and the newest accumulated values in each time bin $\{C_j\}_{K+1}$ are compared with their previous counterparts. The signal processor is seeking significant changes in a time bin $|C_{j,K+M} - C_{j,K}| > \beta_j$, with β_j a threshold value and $M = 1, 2, 3, \dots$, to indicate the possible presence of an intruder. Larger values for β_j give a smaller false alarm rate due to statistical fluctuations, but a greater probability of missing an intruder.

The analytical model used for predicting the coherent OTDR performance treats the scattering centers as a large number of reflectors, each with reflectance r , randomly distributed along the length of the fiber. The return light wave in the fiber which reaches the photodetector is composed of a large number of wave with amplitudes $\{A_n\}$, where A_n represents the contribution from the n 'th reflector. Thus, the resultant amplitudes A_x and A_y for light polarized in the x - and y -directions, respectively, can be written

$$A_x = \sum A_n \cos(\Psi_n) \exp(i\phi_{xn}), \quad (1)$$

$$A_y = \sum A_n \sin(\Psi_n) \exp(i\phi_{yn}) \quad (2)$$

where ϕ_{xn} and ϕ_{yn} are the corresponding phases of the polarization components for the wave returned from the n 'th reflector, Ψ_n determines the relative amplitudes of the x - and y -polarizations for that wave, and the detected power $P = |A_x|^2 + |A_y|^2$. Here, the z -axis corresponds to the axis of the fiber. The assumed random spatial distribution of the reflectors has the effect of randomizing the phases $\{\phi_{xn}\}$ and $\{\phi_{yn}\}$, and it is also assumed that the polarization angles $\{\Psi_n\}$ are random. This latter assumption is justified by the fact that cabled fibers show random birefringence along their lengths.

To simulate the response of the coherent OTDR, it is assumed that the light source is monochromatic at a wavelength of 1.3 μm and that the modulator passes a square pulse of light of width τ . The average spacing δ for the mirrors is taken to be 0.1 m, much less than the spatial resolution of the OTDR. The appropriate value of the mirror reflectance r is determined by noting that the total Rayleigh-scattered power P_R experienced in propagating distance δ is related to the power incident on that section P_i by

$$P_R = \alpha \delta P_i, \quad (3)$$

with α the attenuation factor of the fiber, in units of length^{-1} . Thus, $\alpha = (\text{loss in dB/km})/4.343$. For $\lambda = 1.3 \mu\text{m}$, the empirical loss of 0.43 dB/km corresponds to a value $\alpha = 9.7 \times 10^{-5}/\text{m}$. From eq. (3), it follows that the appropriate value for r is given by

$$r = \alpha \delta F, \quad (4)$$

with F the fraction of the Rayleigh-scattered power which is coupled into the fiber core in the reverse direction. It is easily shown that

$$F = .375 (NA/n_f)^2, \quad (5)$$

with NA the fiber numerical aperture and n_f the fiber refractive index. For a typical fiber with $NA = 0.11$ and $n_f = 1.46$, it follows from (5) that $F = .0021$. Using the numerical values indicated above for these parameters, it follows from (4) that $r = 9.7 \times 10^{-5} \times 0.1 \times .0021 = 2.037 \times 10^{-8}$. Thus, the simulation models the Rayleigh backscattering effect as reflection of the incident light by randomly located mirrors of reflectance 2.037×10^{-8} , with an average spacing between the mirrors of 0.1 m.

The average number of $\langle N_{pj} \rangle$ of photoelectrons in time bin j of temporal width $\alpha\tau$ is calculated based upon the power coupled into the fiber and the various sources of optical loss between the light source and photodetector. The statistical noise in the photodetector then has a quasi-Gaussian distribution with a standard deviation $\sigma = [\langle N_{pj} \rangle + \langle N_{dj} \rangle]^{1/2}$, where $\langle N_{dj} \rangle$ is the average number of dark-current electrons per time bin. The effect of the intruder is modeled as a point phase perturbation $\Delta\phi$; i. e., the phase of the light changes by $\Delta\phi$ in passing through the site of the perturbation. A threshold level β_j is set such that if $|C_{j,K+M} - C_{j,K}| > \beta_j$, for any value of $\Delta\phi$, an alarm is indicated. Here $C_{j,K}$ is the number of photoelectrons, averaged over N pulses, in the absence of a perturbation; and $C_{j,K+M}$ is the corresponding value after the perturbation is applied. The value of the threshold β_j is set to give an acceptably low probability of false alarm due to statistical fluctuations alone; e. g., a statistical false alarm probability of 10^{-10} corresponds to $\beta_j = 6.5 \sigma$.

The simulation used the Monte Carlo method to set the locations of mirrors in the fiber and the polarization of the reflected light from each mirror for each trial. The width of the light pulse τ was chosen to be consistent with the desired spatial resolution, and the threshold levels $\{\beta_j\}$ were determined based upon an assumed statistical false alarm probability of 10^{-10} . The number of photoelectrons in a particular time bin was calculated before and after the phase

perturbation was applied. If the perturbation-induced change in the number of photoelectrons did not exceed the threshold, then a missed intruder was indicated. The number of missed intruders in a total of 10,000 trials was determined for time bins at different ranges. In this manner, the range consistent with a particular range resolution and missed intruder probability was determined.

The following parameter values were used in the simulation:

- wavelength: 1.3 μm
- power coupler from laser into fiber: 40 mW
- fiber attenuation: 0.43 dB/km
- optical loss in optical modulator: 3 dB
- excess loss in fiber coupler: 0.1 dB
- photodetector dark current: 0.1 nA
- photodetector quantum efficiency: 0.8
- polarizer excess loss: 0.2 dB
- number of light pulses N used in computing time-bin averages: 10

In the simulations involving the use of internal mirrors in the fiber, these values were used:

- mirror reflectance: 0.001
- mirror loss: 0.05 dB.

An example of the simulated temporal response of the coherent OTDR based upon Rayleigh backscattering without polarization discrimination is given in Fig. 40. The localized (point) phase perturbation in the fiber produces a change in the OTDR signal over a time period equal to the pulse width τ .

Results of the simulation for the dependence of range resolution on range are given in Figs. 41 and 42. These results clearly show the superiority of the Rayleigh backscattering approach to the one utilizing the internal fiber mirrors for ranges > 2 km. The internal mirror approach without polarization discrimination has an inherent fading problem which occurs when the polarization of the light reflected from one mirror, at the photodetector, is very nearly orthogonal to the polarization of the light reflected from the adjacent mirror. In that case, the effect of the localized phase perturbation on the detected power in a particular time bin (i. e., interferometer fringe visibility) becomes very low, and the probability of missing the intruder is correspondingly increased.

Polarization discrimination eliminates the fading associated with the internal mirror approach, and in this case a greater attenuation is allowable between the laser and photodetector than any of the other three cases. This is because a larger fraction of the incident light is reflected in the fiber, and statistical fluctuations in the reflected power are almost eliminated. However, in comparison with the Rayleigh backscattering cases the greater allowable attenuation is more than offset at longer ranges by increased attenuation in the fiber due to the presence of the mirrors. For example, for 100 m resolution there are 10 mirrors per km which produce an increase in the loss of 0.5 dB/km - 10 times the individual mirror loss of 0.05 dB. Thus, the total fiber loss with mirrors is 0.93 dB/km, vs. only 0.43 dB/km for the Rayleigh backscattering cases. Only for ranges less than 2 km, where the fiber attenuation is less important, does the internal mirror approach with polarization discrimination show better range resolution than the Rayleigh backscattering cases.

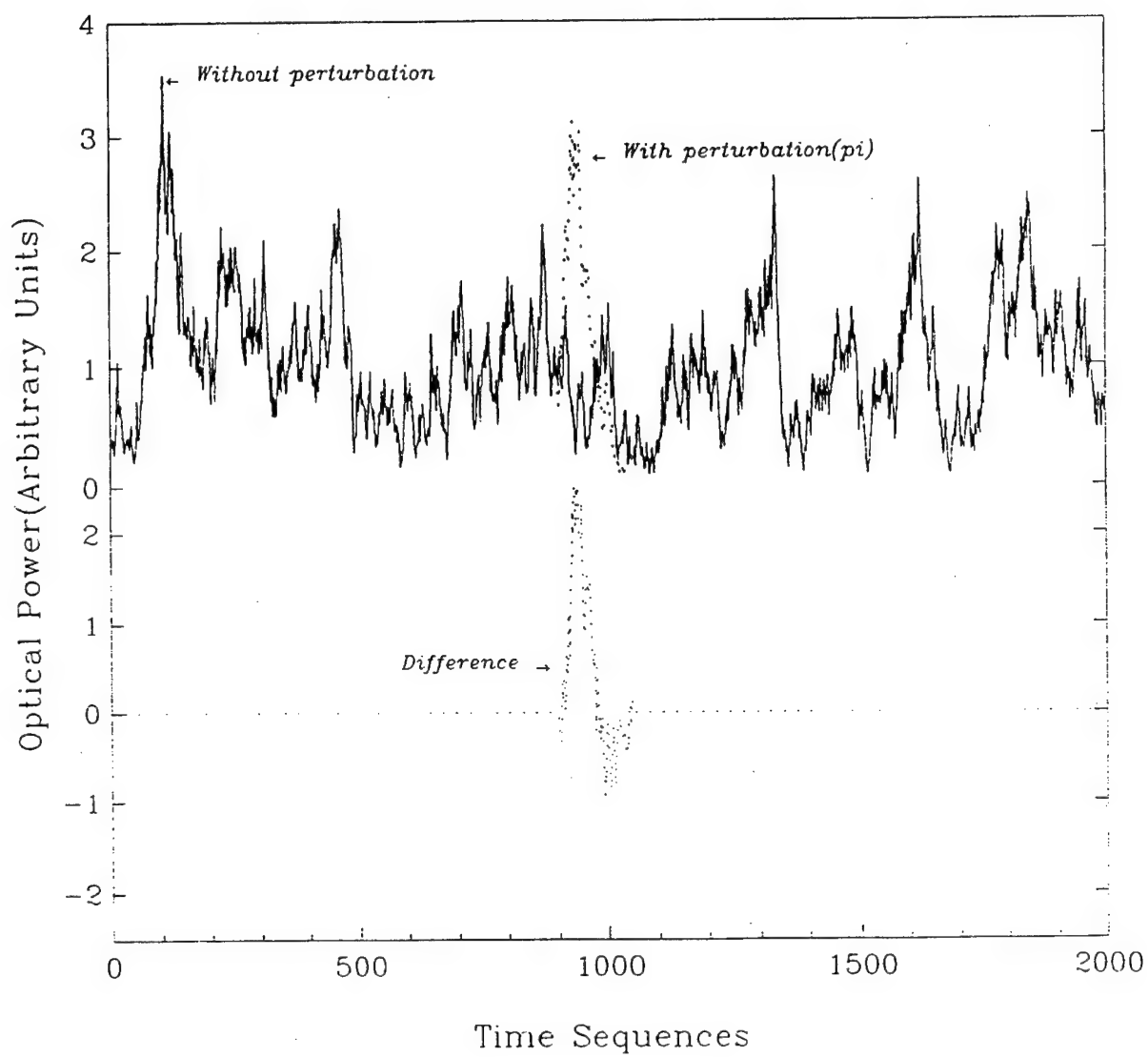


Fig. 40. Coherent OTDR outputs as determined from Monte Carlo simulation, before and after application of a localized π -radian phase perturbation.

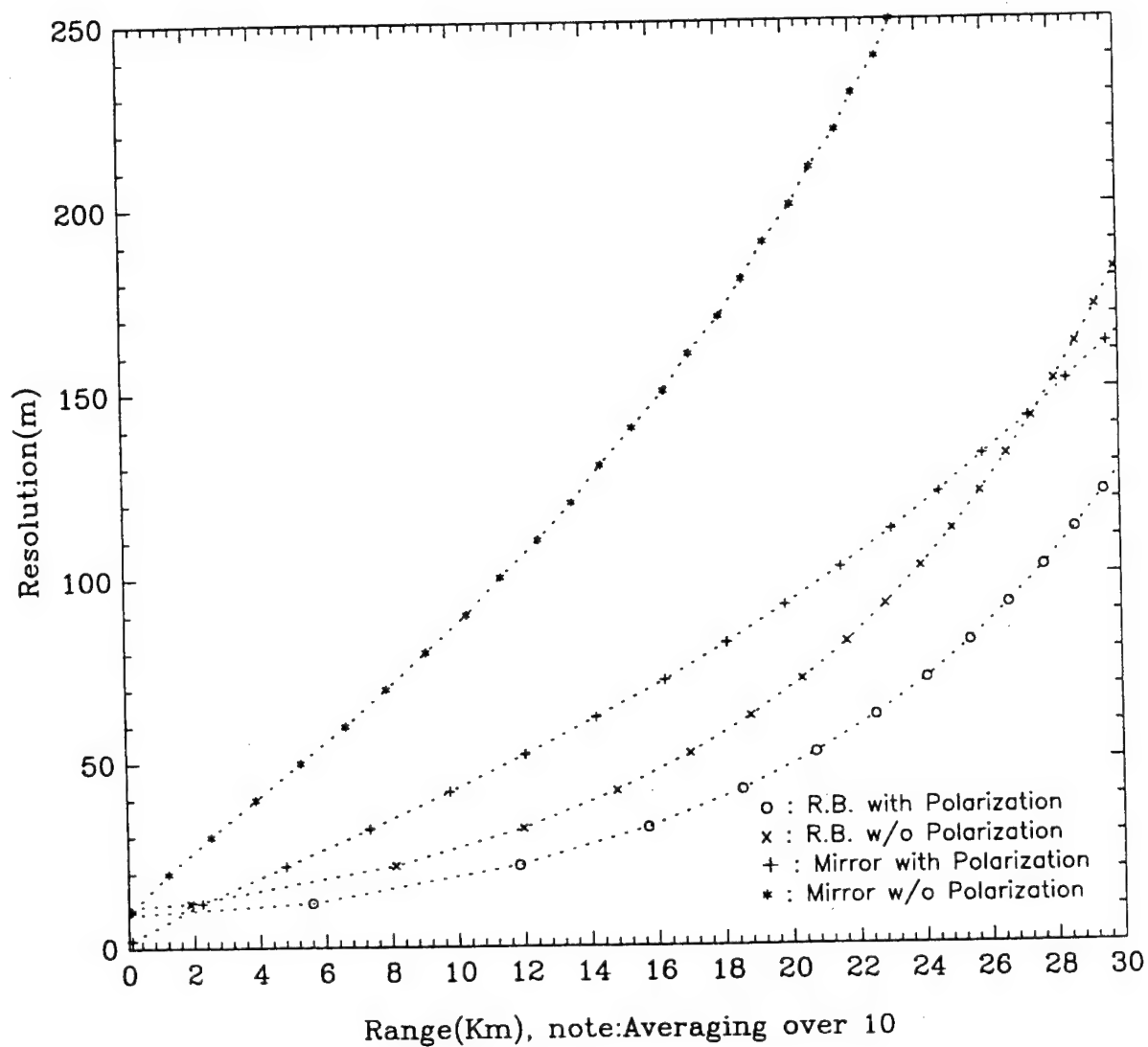


Fig. 41. Dependence of range resolution on range for coherent OTDRs, based upon results of Monte Carlo simulation; statistical false alarm probability = 10^{-10} , missed intruder probability = 10^{-3} .

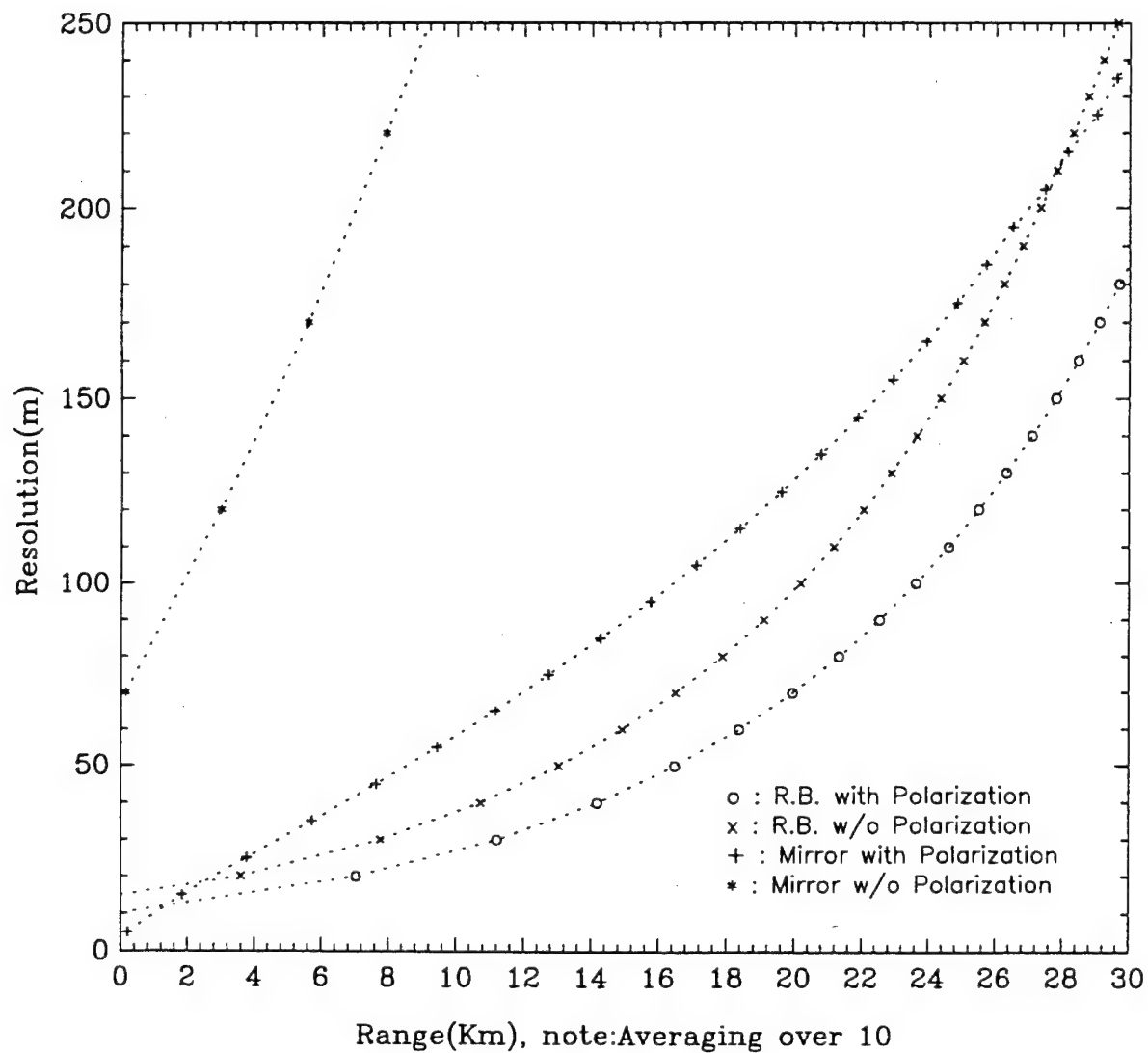


Fig. 42. Same as Fig. 41, but missed intruder probability = 10^{-4} .

For coherent OTDR based upon Rayleigh backscattering, the use of polarization discrimination produces an improvement in range resolution of roughly 50%. Polarization discrimination requires the use of additional components (polarizers, couplers, photodetectors) and leads to a moderate increase in system cost and complexity. It is recommended that both Rayleigh backscattering approaches be explored during the Phase 2 feasibility demonstration.

The results presented above in Figs. 41 and 42 assume that the laser emits a single frequency of light; i. e., that it has perfect spectral purity. Actual lasers, of course, do not meet this ideal, exhibiting a finite linewidth as well as frequency drift with time. From a system design standpoint, the degree of laser stability required is an important issue. The simulations were thus extended to include the effect of laser frequency drift. In particular, for cases considered in Fig. 9, the random frequency change in the laser which causes an effective noise level equal to the shot noise were determined. It is concluded that frequency drift of a commercial laser such as the Model 123-1319-040-F diode-pumped Nd:YAG laser supplied by Lightwave Electronics of Santa Clara, CA, with a specified frequency drift of less than 75 kHz/sec, will not significantly increase the noise of the system.

8. COMPARISON WITH COMPETING INTRUSION SENSOR APPROACHES

Fiber optic systems for intrusion sensing are offered commercially in the United States by three companies: Stellar Systems, Fiber SenSys, and Mason & Hanger. Some of the features of these systems are described below:

Stellar Systems of Santa Clara, CA, a subsidiary of Pilkington in England, markets a line of fiber optic sensors using technology developed by the parent company. One of their products uses a fiber optic strand encased in a steel-barbed tape. The intruder has to break the tape to be detected. The second product is a buried fiber pressure sensor. The fiber can be up to 1 km in length, and the fiber cable is buried about 2" beneath the surface. An intruder stepping on the ground above the cable will be detected as a result of the pressure-induced increase in the attenuation of the buried fiber. Both systems use multimode, step-index fiber and LED light sources.

A somewhat more sophisticated system which uses a semiconductor laser light source and graded-index multimode fiber is offered by Fiber SenSys of Beavertown, Oregon. In this case, the pressure of the intruder causes optical coupling between modes of the fiber. By detecting the change in optical output from part of the fiber core, the intruder is sensed. It is recommended that the sensor cable be deployed in a serpentine manner at a depth of 3" to 6" under gravel.

The system offered by Mason & Hanger of Huntsville, Alabama, system uses ordinary single mode telecommunications fiber. Its configuration is that of a Sagnac interferometer, best known for its use in gyroscopes. The sensing fiber can be as long as 60 km. Its most popular deployment is on fences. For underground deployment, a 4"-6" burial depth is recommended.

With the Mason & Hanger sensor configuration, a phase perturbation in the fiber loop has the same effect on both counterpropagating beams and does not result in a change in the sensor output. Thus, it must be nonreciprocal polarization effects which give the observed signal in response to an intruder. The sensitivity of a sensor which relies upon polarization coupling is orders of magnitude lower than that of an interferometric sensor, which responds to phase perturbations. This explains the relatively shallow burial depth, about the same as for the Stellar

and Fiber SenSys systems which use multimode cable - an indication that interferometric sensitivity is not attained in the Mason & Hanger product.

None of these systems would appear to be cost-effective for monitoring tens or hundreds of km of border terrain. For the Stellar, Fiber SenSys, and Mason & Hanger systems, the sensor determines the presence of an intruder but not his location along the fiber cable. A large number of individual sensor systems would thus be needed to locate intruders to 100 m or less over long perimeters of border terrain. Maintenance of all these systems and transmission of the data to a central processing site would add to the already prohibitive expense. It would be very difficult to maintain covertness because of the large number of terminal boxes required. The 2"-6" burial depth is too shallow to be practical in many areas. The Army/Texas A&M system has the potential to overcome these difficulties. A comparison of the three products with the proposed sensor is given in Table 6.

TABLE 6. COMPARISON OF BURIED FIBER OPTIC INTRUSION SENSORS

	Fiber SenSys	Stellar Systems	Mason & Hanger	Army/Texas A&M
light source type	laser diode	LED	laser diode	Nd: YAG laser
light source λ (μm)	0.8 μm	0.8 μm	1.3 or 1.55 μm	1.3 μm
fiber type	graded-index multimode	step-index multimode	single mode	single mode
photodetector	Si PIN	Si PIN	InGaAs PIN	InGaAs PIN
max. length L (km)	0.6	1.0	60	28 (100 m resolution)* 12 (20 m resolution)*
# sectors/fiber	1	1	1	280-600
burial depth (cm)	7.5 - 15 (under gravel)	5	10-15	30-60**
lateral range (cm)	25	15	not specified	200**

*Based upon simulation results; assumed statistical false alarm probability = 10^{-10} , missed intruder probability = 10^{-3}

**Based upon experiments with a buried Michelson interferometer.

9. CONCLUSIONS

9.1. All-Fiber Switch

A four-port, all-fiber optical switch was developed. The switch was configured as a Mach-Zehnder interferometer, with piezoelectric transducers (PZTs) attached to the two fibers in the interferometer arms. Switching was accomplished by applying appropriate voltages to the two PZTs. The switch exhibited the following characteristics:

operating wavelength: 1.3 μm
optical insertion loss: 0.25 dB
crosstalk: <-21 dB
switching voltage: 57V
switching speed (10%-90%): 8 μsec minimum;
30 μsec for practical application

The all-fiber switch compares favorably with its integrated optic and thermo-optic counterparts [4], [5]. A major drawback of the delay line using integrated optic switches is high insertion loss, which makes multistage switch delay line impractical without signal amplification. A second difficulty with integrated optic switches is the polarization sensitivity, which leads to the requirements of expensive polarization maintaining fiber. With thermo-optic switches, the system reconfiguration time is larger than 2 msec and the switch states are difficult to maintain.

9.2. Programmable Delay Line

An algorithm for a delay line with a multistage 2x2 switches architecture was developed. A 4-stage, 150 nsec programmable delay line with the configuration of Fig. 2 was demonstrated. $2^4 = 16$ different time delays were achieved with four 2x2 all-fiber piezoelectrically actuated optical switches. The system loss was 4.9 dB.

9.3. Distributed Intrusion Sensor

The coherent OTDR fiber optic intrusion sensor offers some revolutionary features not attainable with any other technology. In particular, there is no distributed sensor which provides the means to locate as well as to detect intruders. Referring to Table 6, p. 60, up to 600 sectors can be provided along the length of the fiber cable. The coherent OTDR would thus replace up to 600 individual sensors, as well as the means to transmit the signals from the 600 sensors to a central location for processing.

The second key advantage of the coherent OTDR is its ability to detect an intruder crossing over a cable deployed in linear fashion. This is possible because of the large (2 m) lateral detection range possible only with an interferometric (coherent) sensor. With the other fiber optic sensors of Table 6, the lateral range is limited to a few inches because of the low sensitivity of noninterferometric approaches. The short lateral range means that an intruder can escape

detection by stepping over a linearly deployed cable, so it has to be wound back and forth in serpentine fashion.

The buried deployment of the fiber optic sensor without the need for radio transmission of the sensor information is a major advantage over conventional seismic, infrared, and magnetic intrusion sensors. At an estimated installed cost of about \$5 K / km for long perimeters, the fiber optic system should be more affordable than any of the competing technologies. More uniform perimeter coverage provided by the fiber optic sensor should make it more difficult to defeat than conventional sensors, leading to a lower probability of missing an intruder. The greater quantity of data available for processing by the fiber optic sensor should make it possible to provide better discrimination against animals and other sources of nuisance alarms.

The analysis has shown that, for ranges in excess of 2 km, the best range resolution is provided using the Rayleigh backscattering approach with polarization discrimination. If polarization discrimination is not used, the range resolution degrades (increases) by roughly 50%. Since polarization discrimination requires only a moderate increase in component cost and in the complexity of the signal processing, this will be preferred in most applications.

The performance of the internal mirror approach without polarization discrimination is inferior to the other three cases and does not appear to be practical. The use of internal mirrors with polarization discrimination would appear to have value only for ranges below 2 km, where some improvement in range resolution over the Rayleigh backscattering case might be achieved. However, the considerable increase in cost for the cable could preclude the use of internal mirrors even for short-range systems.

10. REFERENCES

1. K. Wilner and A.P. van den heuvel, "Fiber-optic delay lines for microwave signal processing," *Proc. IEEE*, vol. 64, pp. 805-807, 1976.
2. H.F. Taylor, "Novel applications of fiber optics," in *Fiber Optics: Advances in Research and Development*, B. Bendow and S.S. Mitra, eds, new York, NY: Plenum, 1979, pp. 613-623.
3. H.F. Taylor, S. Gweon, S.P. Fang, and C.E. Lee, "Fiber optic delay-lines for wideband signal processing," *Devices for Optical Processing*, D.M. Gookin, Ed, Proc. SPIE 1562, pp. 264-275, 1991.
4. M. Kawachi, "Silica waveguides on silicon and their application to integrated-optic components," *Opt. and Quantum Electron.*, vol. 22, pp. 291-416, 1990.
5. E. Voges and A. Neyer, "Integrated-optic devices on LiNbO₃ for optical communication," *J. Lightwave Technol.*, vol. LT-5, pp. 1229-1238, 1987.
6. H.F. Taylor and A. Yariv, "Guided wave optics," *Proc. IEEE*, vol. 62, No. 8, pp. 1044-1060, Aug. 1974.
7. M. Kobayashi, H.F. Taylor, K. Takada, and J. Noda, "Optical fiber component characterization by high-intensity and high-spatial-resolution interferometric optical-time-domain reflectometer," *IEEE Photon. Technol. Lett.*, vol 3, pp. 564-566, 1991.
8. J.W. Goodman, *Statistical Optics*. new York: John Wiley & Sons, Inc., 1985.
9. M. Born and E. Wolf, *Principles of Optics*, -6th Ed., Oxford, England: Pergamon Press, 1980.
10. I.P. Kaminow, "Polarization in optical fibers," *IEEE J. Quantum Electron.*, vol. QE-17, pp. 15-22, 1981.
11. S.C. Rashleigh, "Origins and control of polarization effects in single-mode fibers," *IEEE J. Lightwave Technol.*, vol. LT-1, pp. 312-331, 1983.
12. K. Nosu, H.F. Taylor, S.C. Rashleigh, and J.F. Weller, "Acoustic-optic phase modulator for single-mode fibers," *Electron. Lett.*, vol. 19, pp. 605-607, 1983.
13. S.A. Kingsley, "Optical-fiber phase modulator," *Electron. Lett.*, vol. 11, pp. 453-454, 1975.
14. H.F. Taylor, "Acoustic modulators for single-mode fibers," *J. lightwave Technol.*, vol. Lt-5, pp. 990-992, 1987.
15. D.D. Reynolds, *Engineering Principles of Acoustics: Noise and Vibration Control*. Boston, mass: Allyn and Bacon, 1981.
16. M.P. Norton, *Fundamentals of noise and vibration analysis for engineers*. New York; Cambridge University Press, 1989.
17. T. Yoshino, k. Kurosawa, K. Ithoh, and T. OSe, "Fiber-optic Fabry-Perot interferometer and its sensor application," *IEEE J. Quantum electron*, vol. QE-18, pp. 1624-1633, 1982.
18. G.D. Pitt, P. Extance, R.C. Neat, D.N. Batchelder, R.E. Jones, J.A. Barnett, and R. H. Pratt, "Optical-fiber sensors," *IEE Proc.*, vol. 132, pp. 214-248, 1985.
19. T.G. Giallorenzi, J.A. Bucaro, A. Dandridge, G.H. Sigel, Jr., J.H. Cole, and S. C. Rashleigh, "Optical fiber sensor technology," *IEEE J. Quantum Electron.*, vol. QE-18, pp. 626-665, 1982.
20. R.C. Youngquist, L.F. Stokes, and H.J. Shaw, "Effects of normal mode loss in dielectric waveguide directional couplers and interferometers," *IEEE J. Quantum Electron.*, vol. QE-19, pp. 1888-1896, 1983.

21. I.J. Wilkinson, "Wear-out failure mechanism in fused-fiber couplers," *Electron. Lett.*, vol. 29, pp. 1137-1139, 1993.
22. K.P. Jackson, S.A. Newton, B. Moslehi, M. Tur, C. C. Cutler, J.W. Goodman and H.J. Shaw, "Optical fiber delay-line signal processing," *IEEE Trans. Microwave Theory Techn.*, vol. MTT-33, No. 3, pp. 193-209.
23. A.P. Goutzoulis and D.K. Davies, "Hardware-compressive 2-D fiber optic delay line architecture for time steering of phased-array antennas," *Appl. Opt.*, vol. 29, pp. 5353-5359, 1990.
24. C.V. Cryan and C.D. Hussey, "Fused polished singlemode fiber couplers," *Electron. Lett.*, vol. 28, pp. 204-205, 1992.
25. Y. Namihira, T. Kawazawa, and H. Wakabayashi, "Incident polarization angle and temperature dependence of polarization and spectral response characteristics in optical fiber couplers," *Appl. Opt.*, vol. 30, pp. 1062-1069, 1991.
26. D. Hanson and N. Gosset, "Applications of optical switches in fiber optic communication networks," *Fiber Optics in the Subscriber Loop*, L.D. Hutcheson and D.A. Kahn, Eds, Proc. SPIE 1363, pp. 48-56, 1990.
27. H.F. Taylor, "Optical-waveguide connecting networks," *Electron. Lett.*, vol. 10, pp. 41-43, 1974.
28. K. Morishita and T. Tahara, "Wavelength-insensitive couplers in form of all-fiber Mach-Zehnder interferometer," *Electron. Lett.*, vol. 27, pp. 1200-1202, 1991.
29. F. Gonthier, D. Ricard, S. Lacroix, and J. Bures, "Wavelength-flattened 2X2 splitters made of identical single-mode fibers," *Opt. Lett.*, vol. 16, pp. 1201-1203, 1991.
30. S. P. Fang, "Fiber optic delay line development," Ph. D. Dissertation, Texas A&M University, May 1994.
31. S. P. Fang and H. F. Taylor, "High-performance single-mode fiber-optic switch," *Optics Letters*, vol. 19, pp. 1204-1206, Aug. 15, 1994.
32. H. F. Taylor and C. E. Lee, "Apparatus and Method for Fiber Optic Intrusion Sensing," U. S. Patent #5,194,847, issued March 1993.
33. W. Seo, "Fiber optic intrusion sensor investigation," Ph. D. Dissertation, Texas A&M University, August 1994.

MISSION OF ROME LABORATORY

Mission. The mission of Rome Laboratory is to advance the science and technologies of command, control, communications and intelligence and to transition them into systems to meet customer needs. To achieve this, Rome Lab:

- a. Conducts vigorous research, development and test programs in all applicable technologies;
- b. Transitions technology to current and future systems to improve operational capability, readiness, and supportability;
- c. Provides a full range of technical support to Air Force Material Command product centers and other Air Force organizations;
- d. Promotes transfer of technology to the private sector;
- e. Maintains leading edge technological expertise in the areas of surveillance, communications, command and control, intelligence, reliability science, electro-magnetic technology, photonics, signal processing, and computational science.

The thrust areas of technical competence include: Surveillance, Communications, Command and Control, Intelligence, Signal Processing, Computer Science and Technology, Electromagnetic Technology, Photonics and Reliability Sciences.